Journal of *Marine Science and Engineering*

MDPI

Article

Dynamic Structural Behavior of Monopile Support Structure for 15 MW Offshore Wind Turbine During Different Phases of Operation

Sajid Ali [1], Muhammad Waleed [2] and Daeyong Lee [2,*]

[1] Energy Innovation Research Center for Wind Turbine Support Structures, Kunsan National University, 558 Daehak-ro, Gunsan-si 54150, Jeollabuk-do, Republic of Korea; sajid_ali@kunsan.ac.kr
[2] Department of Wind Energy, The Graduate School of Kunsan National University, 558 Daehak-ro, Gunsan-si 54150, Jeollabuk-do, Republic of Korea; waleedmuhammad6555@gmail.com
* Correspondence: daeyong.lee@kunsan.ac.kr; Tel.: +82-10-4490-0980

Abstract: The structural integrity of offshore wind turbine monopiles is critical for ensuring operational stability and long-term performance under varying environmental and aerodynamic loads. However, transient load conditions during different operational phases, such as start, normal stop, and emergency stop, can significantly impact structural behavior, influencing fatigue life and dynamic stability. This study investigates the dynamic structural response of a 15 MW offshore wind turbine monopile, incorporating modal analysis and transient simulations to assess deflection, forces, moments, and rotational displacements at the mud-line. The modal analysis revealed natural frequencies of 0.509492 Hz, 1.51616 Hz, and 3.078425 Hz for the blade's flap-wise modes, while side-to-side modes for the combined tower and monopile structure were identified at 0.17593 Hz, 0.922308 Hz, and 1.650862 Hz. These frequencies are crucial in evaluating resonance risks and ensuring dynamic stability under combined aerodynamic and hydrodynamic forces. The transient analysis demonstrated that lateral force (F_y) variations peaked at −2500 kN during emergency stop, while moment fluctuations (My) reached ±100,000 kNm, reflecting the monopile's high dynamic sensitivity under sudden aerodynamic unloading. Rotational displacements also showed significant variations, with θx oscillating up to ±0.0009 degrees and θy between −0.0022 and −0.0027 degrees. These findings provide valuable insights into optimizing monopile design to mitigate resonance effects, improve fatigue performance, and enhance structural resilience for large-scale offshore wind turbine support systems.

Keywords: transient; monopile; offshore; load; structure; elasticity

check for updates

Academic Editor: Bang-Fuh Chen

Received: 10 February 2025
Revised: 27 February 2025
Accepted: 4 March 2025
Published: 6 March 2025

Citation: Ali, S.; Waleed, M.; Lee, D. Dynamic Structural Behavior of Monopile Support Structure for 15 MW Offshore Wind Turbine During Different Phases of Operation. *J. Mar. Sci. Eng.* **2025**, *13*, 515. https://doi.org/10.3390/jmse13030515

Copyright: © 2025 by the authors. Licensee MDPI, Basel, Switzerland. This article is an open access article distributed under the terms and conditions of the Creative Commons Attribution (CC BY) license (https://creativecommons.org/licenses/by/4.0/).

1. Introduction

The rapid expansion of offshore wind energy has positioned it as a key pillar in global renewable energy strategies, providing an efficient solution for large-scale electricity generation. Offshore wind farms benefit from stronger and more consistent wind speeds compared to their onshore counterparts, resulting in higher capacity factors and improved energy yields (IEC 61400-1 [1]; Katsanos et al. [2]). As the offshore wind industry progresses, there has been a notable shift toward larger-capacity turbines, including next-generation models such as the NREL IEA 15 MW reference turbine, which serves as a benchmark for future offshore wind technology (Asareh et al. [3]; Katsanos et al. [4]). The increasing turbine size, however, introduces significant structural and dynamic challenges, particularly for the foundation systems supporting these massive loads. Among various

foundation types, monopiles dominate the offshore wind market, accounting for nearly 80% of installed capacity worldwide, primarily due to their cost-effectiveness, ease of installation, and structural simplicity (Yang et al. [5]; Santangelo et al. [6]). While monopiles have demonstrated high reliability in supporting offshore wind turbines in shallow to intermediate water depths, the trend toward ultra-large turbines has necessitated a deeper understanding of their dynamic behavior, as they now experience greater aerodynamic, hydrodynamic, and inertial loads (Avossa et al. [7]; Mo et al. [8]).

Existing research has extensively examined the static and fatigue performance of monopiles under steady-state aerodynamic and hydrodynamic loading conditions (Santangelo et al. [9]; Failla et al. [10]). These studies have contributed significantly to the structural design and fatigue life assessment of monopiles, ensuring their stability under uniform environmental forces. However, the influence of transient loading scenarios remains underexplored, particularly those occurring during operational transitions, such as turbine start-up, normal stopping, and emergency shutdown (Zuo et al. [11]; Wang et al. [12]). These transient conditions introduce rapidly varying aerodynamic and hydrodynamic forces, leading to higher structural stresses and deflections compared to steady-state operations. This effect is particularly important when assessing cumulative fatigue damage, as transient phases often impose short-duration peak loads, which can significantly accelerate structural degradation and reduce the service life of the support structure (Ju and Huang [13]; Fan et al. [14]). While extensive studies exist on smaller offshore wind turbines, research addressing the dynamic behavior of large-capacity turbines, such as 15 MW-class models, remains limited (Zuo et al. [15]; De Risi et al. [16]). Given that structural and aerodynamic characteristics differ substantially between smaller and larger turbines, these knowledge gaps underscore the urgent need for detailed transient analyses of large-scale offshore wind systems.

Another major challenge in the monopile design is the complex interaction between the foundation and its surrounding environment during transient operational phases. The soil–structure interaction (SSI) is a crucial factor influencing load distribution, stiffness properties, and energy dissipation, particularly in offshore regions with variable seabed conditions (Kaynia [17]; del Campo et al. [18]). During emergency shutdowns, typically caused by overspeed conditions or sudden gusts, the monopile experiences significant dynamic loads, amplifying the role of SSIs in structural stability (Kitahara and Ishihara [19]; Wang and Ishihara [20]). Additionally, hydrodynamic coupling effects, arising from wave–current interactions, further complicate the structural response, leading to combined aerodynamic and hydrodynamic loading, which can alter stress distributions along both the monopile and the tower. Despite the importance of these effects, previous research has predominantly relied on simplified models and steady-state assumptions, which fail to accurately capture the true transient responses observed in real-world offshore wind farms (Witcher [21]; Bossanyi [22]). Moreover, experimental validation of numerical models remains scarce, limiting confidence in predictive simulations and practical design applications (Jonkman and Buhl [23]; Larsen et al. [24]).

One of the key advancements in recent research is the evaluation of drivetrain technologies for 15 MW turbines to reduce the levelized cost of energy (LCOE). Studies have shown that drivetrain optimization plays a crucial role in determining the economic feasibility of large wind turbines, with new configurations reducing costs to under USD 85/MWh [25]. Additionally, research on aerodynamic and structural analyses of turbine blades has provided insights into optimizing airfoil designs for floating wind turbines, improving their efficiency in high wind speed environments [26].

Mooring system design has also been a major focus for floating offshore wind turbines. A study on the mooring design of 15 MW floating wind turbines in the South China Sea ana-

lyzed the impact of platform dynamics on system stability and load distribution, providing valuable data for the deployment of large-scale floating wind farms [27]. Furthermore, dynamic response studies comparing the installation processes of 5 MW and 15 MW turbines have highlighted the challenges associated with large offshore structures, emphasizing the need for improved installation methodologies to ensure structural reliability [28].

The impact of compressibility effects on the aerodynamic performance of wind turbines has also been investigated, with findings suggesting that air compressibility significantly influences power output efficiency and structural loads in 15 MW turbines [29]. Complementary research has explored the optimization of TetraSpar-type floaters, which offer enhanced stability for floating wind turbines by improving load distribution and reducing fatigue stresses [30].

Operational and maintenance strategies have been another critical research area. Studies comparing the costs of direct-drive and medium-speed offshore wind turbines have provided valuable insights into the economic feasibility of different drivetrain configurations for large wind turbines [31]. Moreover, the flexibility effects of turbine blades on loads and wake dynamics have been analyzed using flexible actuator line models, highlighting the importance of blade design in mitigating structural stresses [32]. Additionally, the effects of yaw error and fault conditions on dynamic responses have been studied extensively, with findings indicating that accurate yaw control is essential for minimizing excessive structural loads and improving turbine lifespan [33].

Several studies have also focused on the hydrodynamic performance of floating offshore wind turbines. Research on wave-induced loads and floating platform dynamics has demonstrated that semisubmersible platforms offer improved stability and load distribution compared to conventional monopile foundations, particularly for 15 MW turbines operating in extreme wave conditions [34]. Furthermore, wind tunnel and wave basin experiments have validated numerical models for floating offshore wind turbine dynamics, reinforcing the need for experimental verification in large turbine design [35].

In the field of control systems, LIDAR-assisted feedforward pitch control has been investigated as a strategy for optimizing the performance of floating offshore wind turbines. This approach has been found to improve load mitigation and increase power efficiency, making it a promising technology for future large-scale deployments [36]. Additionally, studies on multi-objective optimization of individual pitch control strategies have demonstrated their effectiveness in reducing fatigue loads and enhancing turbine longevity [37].

Advanced tower and foundation designs have also been explored, with research focusing on prestressed precast UHPC-steel hybrid towers for supporting 15 MW turbines. These hybrid structures have been shown to enhance load-bearing capacity and resistance to dynamic loads, making them a viable solution for next-generation offshore wind farms [38]. Furthermore, dynamic response studies of floating wind turbines with non-redundant mooring systems have provided insights into stability improvements under extreme environmental conditions, contributing to the development of more resilient offshore wind turbine structures [39].

Most recent studies in 2025 have provided further insights into the aerodynamic, structural, and operational aspects of large-scale offshore wind turbines, particularly focusing on 15 MW-class models. Gu et al. [40] investigated the power performance and dynamic characteristics of a 15 MW floating wind turbine integrated with a wave energy converter, highlighting the potential for hybrid renewable energy systems to improve efficiency and resilience. Their study demonstrated that the combined system achieved improved power stability in varying oceanic conditions. Similarly, Chuang et al. [41] explored structural nonlinearity effects on the aeroelastic and wake characteristics of a 15 MW turbine, reveal-

ing that large-scale wind turbines exhibit significant wake deformation due to aerodynamic nonlinearity effects, which must be accounted for in advanced simulation models.

Structural flexibility remains a crucial aspect of floating wind turbines. Lee et al. [42] studied the impact of hull flexibility on the global performance of a 15 MW concrete-spar floating offshore wind turbine. Their results indicated that hull flexibility significantly alters dynamic performance, influencing motion response and fatigue life. Similarly, Bian et al. [43] conducted a dynamic response analysis of alternative mooring systems for a 15 MW floating wind turbine, emphasizing that different mooring designs influence platform stability, particularly under extreme environmental loading conditions. These findings reinforce the need for optimized mooring system designs tailored to site-specific wind and wave conditions.

Control strategies have also been a key focus of recent research. Jeon et al. [44] performed a parametric analysis of control techniques for a 15 MW semisubmersible floating wind turbine, assessing the effectiveness of advanced control algorithms in mitigating structural loads and improving energy capture. In addition, Martínez et al. [45] investigated black-start control strategies for a 15 MW offshore wind turbine, exploring the feasibility of restarting turbines in islanded power grid scenarios. Their findings highlight the importance of self-starting capabilities in large-scale offshore wind farms, particularly for grid stability.

Structural integrity under extreme environmental conditions is another critical research area. Bozyigit et al. [46] conducted a rapid assessment of seismic performance for large monopile-supported offshore wind turbines under scour conditions. Their study provided valuable insights into monopile stability under earthquake-induced seabed deformations, suggesting the need for enhanced foundation reinforcement strategies in seismically active offshore regions. Furthermore, He et al. [47] performed a numerical investigation of second-order sum-frequency wave forces on a 15 MW tension-leg platform (TLP) floating wind turbine, demonstrating that mooring fatigue significantly increases under high-frequency wave loading conditions, necessitating fatigue-resistant mooring designs.

The existing body of research on offshore wind turbine support structures has primarily focused on steady-state loading conditions, leaving a significant gap in understanding the transient dynamic behavior during critical operational phases such as start-up, normal stop, emergency stop, and parked conditions. While previous studies have explored fatigue and stability under extreme environmental loads, the intricate interaction of the tower and monopile with environmental loads during transient events remains insufficiently addressed. Additionally, conventional analyses often rely on oversimplified assumptions, such as simulated wind or wave conditions, which fail to capture the actual dynamic structural responses observed in real-world scenarios.

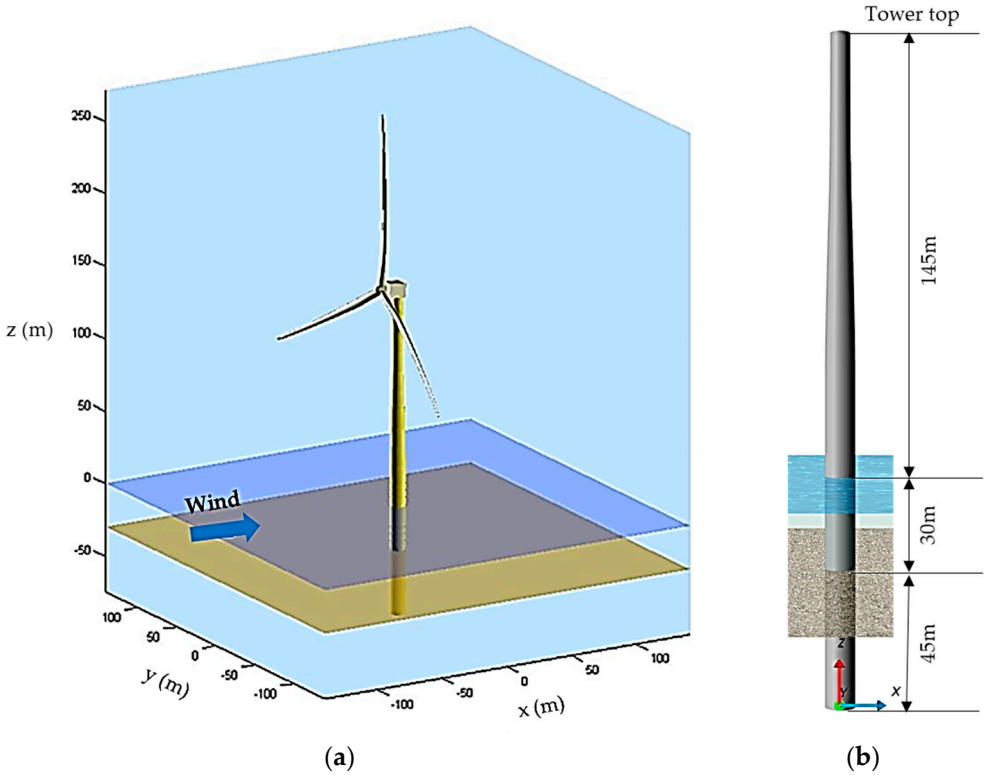
This study bridges these gaps by conducting a detailed transient simulation of the 15 MW offshore wind turbine's tower and monopile support structure across different operational phases. By integrating advanced simulation techniques, this work provides a novel framework for assessing the temporal evolution of forces, moments, and deflections, offering unprecedented insights into structural behavior under transient conditions. The focus on operational phases, coupled with an in-depth analysis of time-dependent interactions, sets this research apart and contributes to the development of more robust and reliable offshore wind turbine designs.

2. Materials and Methods

2.1. Wind Turbine Model

The NREL IEA 15 MW offshore wind turbine, widely recognized as a benchmark for next-generation offshore wind energy systems, is utilized in this study. The turbine model,

including its structural and aerodynamic components, was developed in the BLADED simulation software (version 4.15) to accurately evaluate its dynamic structural response under transient operational conditions. Figure 1 illustrates the 3D numerical representation of the turbine, which consists of the full structural model (Figure 1a) and a detailed depiction of the tower and monopile foundation (Figure 1b).



(**a**) (**b**)

Figure 1. A 3D numerical model of NREL IEA 15 MW wind turbine in BLADED: (**a**) full model; (**b**) tower only (Note: blue layer is water and brown layer is mud-line in (**a**)).

The full turbine model (Figure 1a) incorporates critical components such as the rotor, nacelle, tower, and monopile foundation, providing a holistic framework for analyzing transient loading conditions during start-up, stopping, emergency braking, and parked phases. The aerodynamic loads were simulated by applying steady and transient wind conditions to the rotor, while hydrodynamic forces from waves and currents were applied to the monopile.

The important parameters of the wind turbine used in this study are based on the publicly available NREL IEA 15 MW reference wind turbine model [48]. However, the numerical modeling, transient load analysis, and all simulations presented in this study were independently developed and executed using BLADED software, which is a widely recognized tool for the aero-hydro-elastic analysis of offshore wind turbines. Therefore, the detailed evaluation of dynamic structural responses under varying operational phases, including start-up, normal stop, emergency stop, and parked conditions, is allowed for.

The monopile structure, a cylindrical steel foundation with a diameter of 10 m, extends 45 m into the seabed and 30 m above the sea surface (Figure 1b). The tower, standing 145 m tall from the monopile's base to the rotor's hub height, is modeled with varying wall thickness to optimize structural performance under different loading scenarios. The boundary conditions include fixed constraints at the seabed and a coupled interaction between the tower and the monopile, ensuring accurate load transfer during transient simulations. This comprehensive model enables a detailed evaluation of the turbine's structural behavior and integrity during its operational phases.

In this study, the structural and inertial properties used for modeling the NREL IEA 15 MW wind turbine in BLADED were derived from publicly available NREL datasets, along with estimations based on material properties and engineering calculations. The key parameters considered include the rotor diameter of 240 m, hub height of 150 m, and a total turbine mass of approximately 1.2×10^7 kg, as mentioned in Table 1. The dynamic characteristics, including the first and second natural frequencies (0.179 Hz and 0.922 Hz, respectively), were computed using BLADED simulations. Damping ratios and moments of inertia for the key components were also derived from the simulation results to accurately capture the dynamic response under operational and transient loading conditions. This comprehensive dataset ensures a high-fidelity representation of the wind turbine structure in the numerical simulations.

Table 1. Structural and inertial properties.

Property	Value	Source
Rotor Diameter (m)	240	NREL IEA 15 MW
Hub Height (m)	150	NREL IEA 15 MW
Total Turbine Mass (kg)	1.2×10^7	Derived from NREL data
Blade Mass (kg)	120,000	NREL IEA 15 MW
Nacelle Mass (kg)	800,000	NREL IEA 15 MW
Tower Mass (kg)	4.5×10^6	Estimated from material data
Monopile Mass (kg)	6.0×10^6	Estimated from material data
First Natural Frequency (Hz)	0.179	BLADED simulation
Second Natural Frequency (Hz)	0.922	BLADED simulation
Damping Ratio (%)	2.5	BLADED settings
Moment of Inertia (Blade) (kg·m^2)	3.2×10^7	BLADED simulation
Moment of Inertia (Nacelle) (kg·m^2)	1.8×10^8	BLADED simulation
Moment of Inertia (Tower) (kg·m^2)	2.5×10^9	BLADED simulation

It should be mentioned that the BLADED software, while being one of the most widely used tools for offshore wind turbine simulations, has certain limitations in modeling fully coupled aero-hydro-soil interactions with high-fidelity computational accuracy. The model primarily relies on linearized soil stiffness matrices, which do not fully capture nonlinear soil–structure interactions under varying cyclic loading conditions. Additionally, wave–current interactions are included using predefined spectral models rather than fully resolved computational fluid dynamics (CFD) simulations, which may introduce some approximations in hydrodynamic load predictions. Moreover, the structural damping and fatigue life assessments are based on predefined empirical coefficients, which, although validated in industry practices, could be refined further using site-specific experimental validation. Despite these limitations, the model is sufficient for accurately capturing the transient structural behavior of the monopile foundation under operational and extreme loading conditions.

2.2. Analysis Conditions

The dynamic behavior of the monopile support structure was evaluated under four distinct operational phases: start, normal stop, emergency stop, and parked. Each phase incorporates unique operational parameters to simulate real-world scenarios with high accuracy. Tables 2–5 summarize the control logic and parameter settings for these phases, emphasizing their impact on aerodynamic and structural loads.

Table 2. Properties of 'Start' logic.

Parameter	Value	Description
Initial Rotor Speed	0 rpm	The turbine starts from rest, with no initial rotor movement.
Initial Pitch Angle	90 deg	Blades are fully feathered to minimize aerodynamic loads during start-up.
Initial Pitch Rate During Start-Up	1 deg/s	The blades pitch gradually toward the optimal operating position.
Generator Speed at Which Generator is Put Online	5 rpm	The generator connects to the grid when the rotor reaches 5 rpm.
Final Pitch Angle in Start-Up Mode	0 deg	The blades are positioned for maximum aerodynamic efficiency at the end of start-up.

Table 3. Properties of 'Normal Stop' logic.

Parameter	Value	Description
Emergency Pitch Trip Mode	Overspeed	Emergency stop is triggered by rotor overspeed.
Rotor Overspeed Trip for Start Pitching	7 rpm	The rotor speed threshold that initiates blade pitch adjustment.
Emergency Pitch Rate	5 deg/s	The rate at which the blades pitch to the feathered position during an emergency.
Final Pitch	90 deg	Blades are fully feathered to minimize aerodynamic loads during the stop.
Emergency Shaft Brake Trip Mode	Overspeed	Shaft brake is activated based on rotor overspeed conditions.
Rotor Overspeed Trip for Brake Application	7.56 rpm	The rotor speed at which the shaft brake engages to assist in stopping.
Rotor Speed for Brake Application for Parking	2 rpm	The rotor speed at which the brake fully engages for parking the turbine.

Table 4. Properties of 'Emergency Stop' logic.

Parameter	Value	Description
Emergency Pitch Trip Mode	Overspeed	Emergency stop is triggered by rotor overspeed.
Rotor Overspeed Trip for Start Pitching	7 rpm	The rotor speed threshold that initiates blade pitch adjustment.
Emergency Pitch Rate	5 deg/s	The rate at which the blades pitch to the feathered position during an emergency.
Final Pitch	90 deg	Blades are fully feathered to minimize aerodynamic loads during the stop.
Emergency Shaft Brake Trip Mode	Overspeed	Shaft brake is activated based on rotor overspeed conditions.
Rotor Overspeed Trip for Brake Application	7.56 rpm	The rotor speed at which the shaft brake engages to assist in stopping.
Rotor Speed for Brake Application for Parking	2 rpm	The rotor speed at which the brake fully engages for parking the turbine.

During the **start phase** (Table 2), the wind turbine begins operation from a stationary state. The initial rotor speed is set to 0 rpm, with blades fully feathered at a pitch angle of 90 degrees to minimize aerodynamic loads. As the turbine ramps up, the blades pitch gradually at a rate of 1 deg/s toward their optimal aerodynamic position. Once the rotor reaches 5 rpm, the generator is connected to the grid, and the final pitch angle is adjusted to 0 degrees, enabling maximum aerodynamic efficiency for energy generation.

Table 5. Properties of 'Parked' logic.

Parameter	Value	Description
Pitch Angle When Parked	90 deg	Blades are fully feathered to minimize aerodynamic forces during parked state.
Rotor Azimuth When Parked	0 deg	The rotor is aligned at the default azimuth position, typically 0 degrees.
Brake Engagement	Fully Engaged	The shaft brake is engaged to keep the rotor stationary.

The **normal stop phase** (Table 3) represents a gradual deceleration of the wind turbine under controlled conditions. During this phase, the rotor speed and blade pitch are adjusted incrementally to minimize structural stresses while transitioning to a stationary state. The final pitch angle is feathered to 90 degrees, ensuring that aerodynamic forces are reduced to a minimum before the rotor comes to a complete stop. This phase is essential for routine shutdowns during non-emergency conditions.

The **emergency stop phase** (Table 4) is activated in response to overspeed conditions. When the rotor speed exceeds 7 rpm, blade pitching begins at a rate of 5 deg/s until a fully feathered position (90 degrees) is achieved. Simultaneously, the shaft brake is engaged at a rotor speed threshold of 7.56 rpm, providing additional braking to stop the rotor. This phase is critical for minimizing aerodynamic and mechanical stresses during sudden shutdowns caused by extreme environmental or operational conditions.

The **parked phase** (Table 5) represents a stationary state in which the turbine is not operational. The blades are fully feathered at a pitch angle of 90 degrees, and the shaft brake is fully engaged to keep the rotor stationary. The rotor is aligned at a default azimuth position of 0 degrees to minimize aerodynamic forces.

By systematically defining these operational parameters and their associated logic, this study ensures a comprehensive evaluation of the transient structural responses of the monopile and tower under varying conditions. These settings serve as the foundation for the transient simulations conducted in this research.

2.3. Wind and Wave

Table 6 presents the wind characteristics recorded at the Buan region in the Republic of Korea, measured at the hub height of the NREL IEA 15 MW wind turbine. The data spans from 2017 to 2023, capturing key parameters such as wind angle, average wind speed, maximum wind speed, turbulence intensity, and the Weibull distribution parameters k and c.

Table 6. Wind characteristics of Buan at wind turbine hub height.

Year	Wind Angle (deg.)	Avg. Wind Speed (m/s)	Max. Wind Speed (m/s)	TI (−)	k (−)	c (m/s)
2017	191.57	7.74	18.86	0.49	2.19	8.74
2018	174.76	7.47	18.10	0.47	2.27	8.44
2019	200.94	7.61	19.07	0.49	2.15	8.59
2020	192.15	8.07	20.68	0.51	2.06	9.11
2021	184.39	8.26	20.21	0.49	2.17	9.32
2022	176.90	7.97	20.22	0.51	2.06	8.99
2023	190.49	7.71	20.50	0.53	1.98	8.70
Mean (2017–2023)	187.31	7.83	19.66	0.50	2.13	8.84

The mean wind angle over the seven-year period is approximately 187.31 degrees, indicating a consistent wind direction. The average wind speed across these years is 7.83 m per second, while the maximum recorded wind speed reaches 19.66 m per second. These values reflect moderate wind conditions, suitable for offshore wind energy generation. The turbulence intensity, with a mean value of 0.50, indicates a stable flow regime with relatively low turbulence, essential for minimizing structural fatigue in the wind turbine.

The Weibull parameters k and c, with mean values of 2.13 and 8.84 m per second, respectively, further characterize the wind speed distribution. The shape parameter k signifies a narrow wind speed range, while the scale parameter c represents the most probable wind speed. These metrics are vital for defining accurate input conditions for aerodynamic and structural simulations, ensuring reliable predictions of the turbine's dynamic behavior.

This comprehensive wind dataset serves as a critical input for the transient simulations conducted in this study, allowing for a realistic assessment of the monopile support structure's performance under varying environmental conditions. It should also be noted that, despite the observed fluctuations, the variability in wind parameters over the six-year period is relatively small. This suggests that Buan experiences consistent wind conditions, making it a reliable location for offshore wind energy deployment. The minor interannual variations further support the robustness of the wind resource, ensuring predictable loading conditions for offshore wind turbine structures.

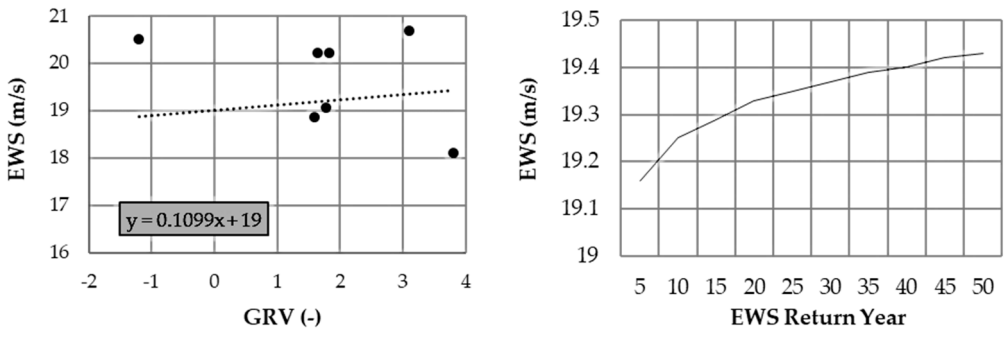
The figures below are the plots of the following set of equations, in which the variable x is the maximum value of wind speed, i.e., the *EWS*, selected from the time series of observations for each time period, and the variable y is the Gumbel reduced variate (*GRV*).

$$x = \alpha y + \beta \tag{1}$$

$$y = GRV = y_{Gumbel} = -ln\{-ln[F(x)]\} \tag{2}$$

$$t = \frac{1}{1 - F(x)} \tag{3}$$

where $F(x)$ is the probability that the annual maximum wind speed is less than x. $F(x)$ can be estimated for each of the observed annual maxima, by simply ordering the data from the smallest (x_1) to the largest (x_n), and calculating an empirical value of $F(x_m)$ from the ranked position of x_m. For every value of x, there is one value of $F(x)$; hence, for each value of x, there is one value of the *GRV* as well. In Equation (1), α is called the scale parameter (also known as dispersion), whereas β is the location parameter (also known as the mode of the extreme value distribution). Both these parameters are symbolic and must be estimated from the Gumbel plot, as shown in Figure 2a (α is the slope and β is the y-intercept of the Gumbel plot, respectively).



(**a**) (**b**)

Figure 2. Estimation of the *EWS*: (**a**) Gumbel plot; (**b**) 50-year return gust.

Figure 2 illustrates the estimation of extreme wind speeds (*EWS*s) for the Buan region using the Gumbel distribution. Figure 2a represents the Gumbel plot, which is used to determine the relationship between the *EWS* and the Gumbel reduced variate (*GRV*). The linear trendline equation, y = 0.1099x + 19, demonstrates the incremental relationship between the *GRV* and *EWS*, with the *EWS* increasing as the *GRV* increases. This analysis forms the basis for predicting the probability of extreme wind events based on historical data. Figure 2a presents the relationship between the *GRV* and *EWS*, with a linear regression model used to fit the observed data. The fitted equation, $EWS = 0.1099 \times GRV + 19$, indicates a weak correlation, suggesting that, while the *GRV* plays a role in influencing the *EWS*, additional meteorological and environmental factors may also contribute significantly. The use of 7 years of measured data is justified based on established statistical methods, including Gumbel's Extreme Value Theory, which has been widely applied in offshore wind energy studies for long-term extreme wind estimation. The approach aligns with industry practices, where datasets spanning 5 to 10 years are commonly used for predicting 50-year extreme wind speeds. Future studies could explore alternative regression models or incorporate additional parameters to improve predictive accuracy.

Figure 2b depicts the 50-year return gust, showcasing the expected *EWS* values over various return periods. For the 50-year return period, the predicted *EWS* is approximately 19.5 m per second, representing the maximum wind speed expected under extreme conditions. This value is critical for designing offshore wind turbine support structures to withstand such rare but intense wind events.

These results provide a robust foundation for defining input conditions in the transient simulations conducted in this study. The combination of Gumbel analysis and return period estimation ensures that the monopile and tower designs are resilient under extreme wind loading scenarios.

The wind speed frequency, known as the Weibull probability density function (*PDF*) ($f(v)$), and the total wind speed frequency, known as the cumulative distribution function (*CDF*) ($F(v)$), as given in the following two equations, can be mathematically defined as follows, respectively:

$$PDF = f(v) = \left(\frac{k}{c}\right)\left(\frac{v}{c}\right)^{k-1} exp\left[-\left(\frac{v}{c}\right)^{k}\right] \qquad (v > 0; k, c > 0) \tag{4}$$

$$CDF = F(v) = 1 - exp\left[-\left(\frac{v}{c}\right)^{k}\right] \qquad (v > 0; k, c > 0) \tag{5}$$

where v is the instantaneous wind speed, k and c and are the Weibull distribution parameters known as the shape and scale factors. Unlike wind speed, Weibull shape and scale factors cannot be directly measured, but complicated mathematical modeling of measured wind speed is required to determine k and c. The accuracy of wind speed data predicted by the Weibull algorithm largely depends on the method used to calculate it. Several analytical and numerical simulation models have been devolved so far to estimate, but the empirical method is the most accurate and, therefore, is used in the present study to estimate these Weibull parameters.

Figure 3 depicts the Weibull distribution for the measured wind speeds at the Buan region, represented by the probability density function (*PDF*) and cumulative distribution function (*CDF*). The *PDF* curve illustrates the likelihood of specific wind speed occurrences, peaking around 7 to 9 m per second, which corresponds to the most frequent wind speed range. The *CDF* curve, on the other hand, shows the cumulative probability of wind speeds not exceeding a given value, approaching 1 as the wind speed increases. This dual representation provides valuable insights into the wind speed distribution, essential for

characterizing the wind regime and optimizing the aerodynamic and structural design of offshore wind turbines.

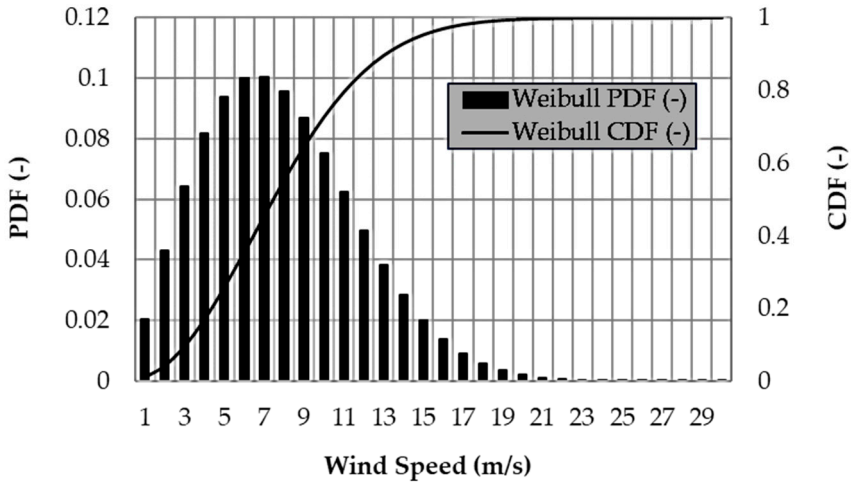


Figure 3. Weibull distribution for measured wind speed.

Figure 4 illustrates the environmental loads acting on the offshore wind turbine with respect to direction. Figure 4a presents the wind speed distribution at the hub height, indicating a predominant wind direction around 180 to 200 degrees, with the highest frequency of wind speeds exceeding 6 m per second. Figure 4b shows the significant wave height distribution, where waves primarily align with the wind direction, with most heights ranging between 1 and 3 m. These directional load patterns are crucial for designing the monopile and tower to withstand combined aerodynamic and hydrodynamic forces during varying operational phases.

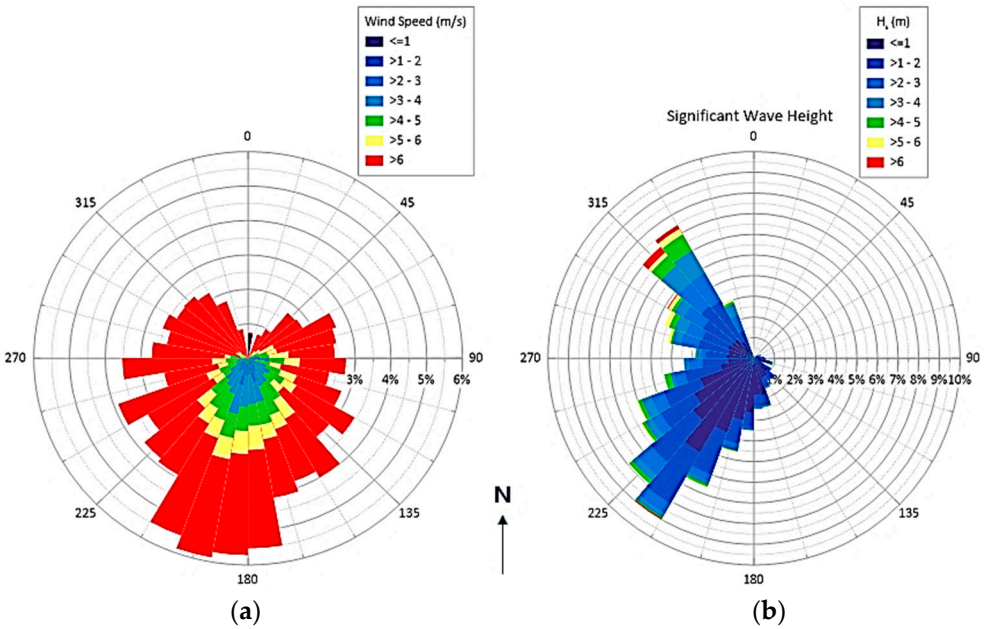


Figure 4. Environmental loads with direction: (**a**) wind speed at hub height; (**b**) significant wave height.

Figure 5 presents the monthly variation in wave cycle duration (in seconds) measured at Buan. The data reveal seasonal fluctuations in wave conditions, with the highest wave cycle observed in April, reaching approximately 12 s, indicating longer wave periods during this month. The wave cycle remains relatively stable for most of the year, fluctuating

between 7 and 10 s, except for notable peaks in April and June, where it exceeds 10 s. March records the shortest wave cycle, suggesting relatively shorter-period waves during early spring. The variations in wave cycles provide critical insight into the hydrodynamic conditions influencing offshore structures, particularly monopile-supported wind turbines, by affecting wave-induced loading patterns. Understanding these variations is essential for assessing the dynamic response of offshore wind turbine foundations and optimizing structural designs to withstand seasonal changes in wave loading.

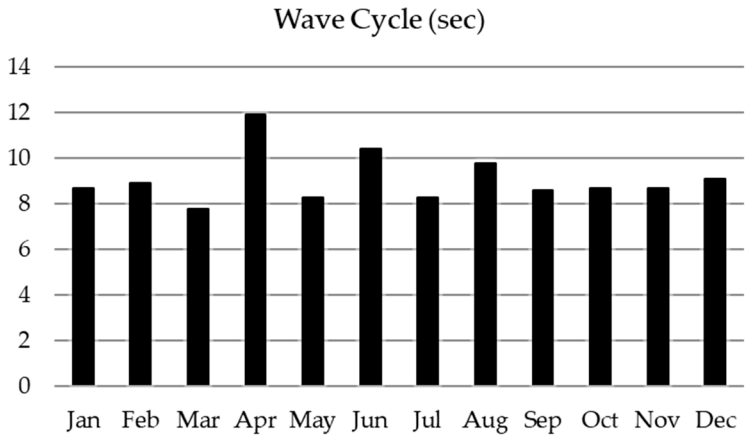


Figure 5. Monthly wave cycle at Buan (measured data).

2.4. Soil Conditions

Table 7 presents the soil stiffness matrix implemented in BLADED, incorporating force–displacement and moment–rotation relationships to account for the monopile's interaction with the seabed. The matrix defines the stiffness coefficients for translational displacements (Δx, Δy, Δz) and rotational displacements (θx, θy, θz) in response to applied forces (Fx, Fy, Fz) and moments (Mx, My, Mz). This stiffness matrix is specified at the mud-line.

Table 7. Soil stiffness matrix entered in BLADED.

	Δx	**Δy**	**Δz**	**θx**	**θy**	**θz**
Fx	1.57×10^9	0	0	0	-2.66×10^{10}	0
Fy	0	1.57×10^9	0	2.66×10^{10}	0	0
Fz	0	0	1.33×10^9	0	0	0
Mx	0	2.66×10^{10}	0	6.85×10^{11}	0	0
My	-2.66×10^{10}	0	0	0	6.85×10^{11}	0
Mz	0	0	0	0	0	1.97×10^{11}

The diagonal elements represent the primary stiffness values, where the horizontal translational stiffness in the x and y directions is 1.57×10^9 N/m, while the vertical translational stiffness in the z direction is slightly lower at 1.33×10^9 N/m. These values indicate the seabed's resistance to monopile movement under axial and lateral loads. The rotational stiffness about the x and y axes is 6.85×10^{11} Nm/rad, ensuring significant resistance to bending moments. Similarly, the rotational stiffness about the *z*-axis is 1.97×10^{11} Nm/rad, reflecting the seabed's torsional resistance.

Off-diagonal coupling terms highlight interactions between different load components. Notably, a coupling term of -2.66×10^{10} N/m is observed between Fx and θy, and between Fy and θx, indicating a strong interdependence between horizontal forces and rotational displacements. Additionally, Mx and Δy exhibit coupling with a stiffness value of 2.66×10^{10} Nm/m, emphasizing the influence of lateral translation on monopile bending moments.

These stiffness values play a critical role in defining the monopile's dynamic response under transient and steady-state conditions. By incorporating these parameters into BLADED, the simulation ensures an accurate representation of soil–structure interaction effects, which is essential for predicting the monopile's load distribution, deflections, and overall structural stability under varying environmental loads.

The stiffness properties used in this study were obtained from a previously published work [48], where detailed calculations and validations were performed. Since these calculations require extensive derivations and discussions, they were not repeated in this paper to maintain the focus on the transient dynamic response of the monopile-supported wind turbine. In BLADED, only stiffness matrices can be directly incorporated into the simulation setup, rather than the full set of soil properties, making it necessary to use precomputed stiffness parameters. The inclusion of these validated stiffness values ensures the reliability of the numerical model without unnecessary duplication of previously established methodologies.

3. Results

3.1. Support Structure Modal Analysis

Figures 6 and 7 present the results of the modal analysis conducted on the NREL IEA 15 MW offshore wind turbine's structural components, including the blade, tower, and monopile. In Figure 6, the modal frequencies for a single blade are illustrated, highlighting the first, second, and third flap-wise modes at 0.509492 Hz, 1.51616 Hz, and 3.078425 Hz, respectively. These modes capture the natural vibration characteristics of the blade, critical for evaluating resonance risks under dynamic wind loading.

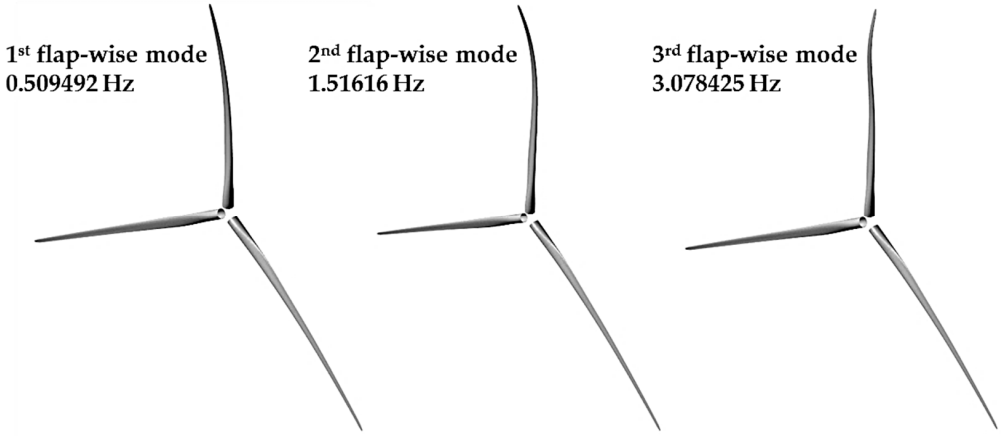


Figure 6. Modal analysis results for single blade.

Figure 7 depicts the side-to-side modes for the combined tower and monopile structure. The first, second, and third modes occur at 0.17593 Hz, 0.922308 Hz, and 1.650862 Hz, respectively. These frequencies are vital for assessing the structural stability and dynamic performance under combined aerodynamic and hydrodynamic forces. The results demonstrate the importance of ensuring that the turbine's operational frequencies do not align with these natural modes to prevent amplification effects and potential structural failure.

The natural frequencies computed in the present study have been validated against the NREL IEA 15 MW wind turbine reference report [49]. However, the reference provides only the first modal frequency for both the blades and tower–monopile system, whereas the present study extends this analysis to the first three modal frequencies. The first tower mode frequency obtained in BLADED is 0.17593 Hz, which shows a 3.49% difference compared to the reported 0.17 Hz in the reference. Similarly, the first blade mode frequency obtained is 0.509492 Hz, reflecting an 8.19% difference from the reported 0.555 Hz in the

NREL IEA 15 MW report. These deviations are within an acceptable range and can be attributed to differences in numerical modeling approaches, meshing techniques, and software-specific computational methods.

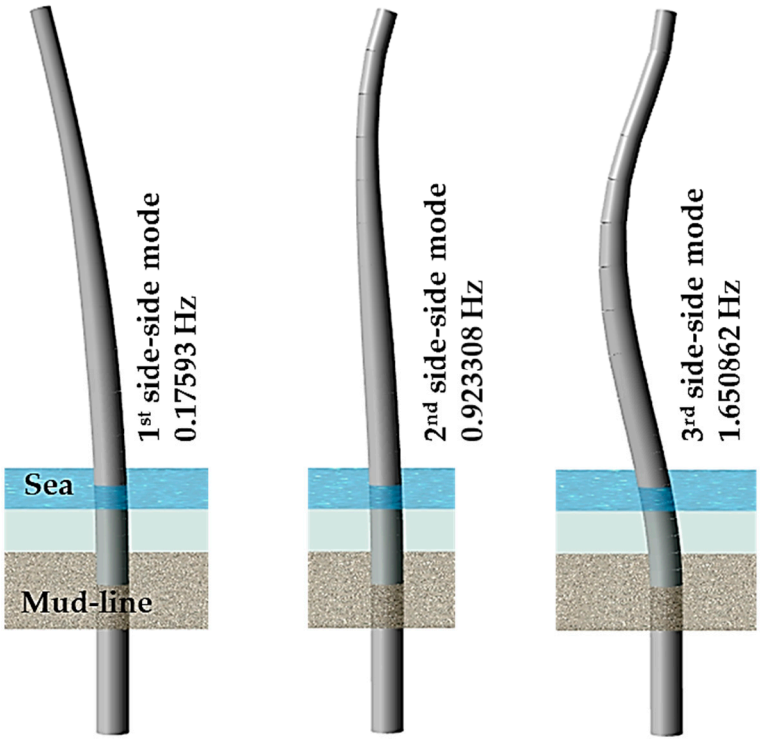


Figure 7. Modal analysis results for tower and monopile combined.

Figure 8 illustrates the tower's lateral oscillation amplitude over time for four operational phases: start, normal stop, emergency stop, and parked. Significant differences in the oscillation patterns are observed, reflecting the varying structural responses under distinct operating conditions.

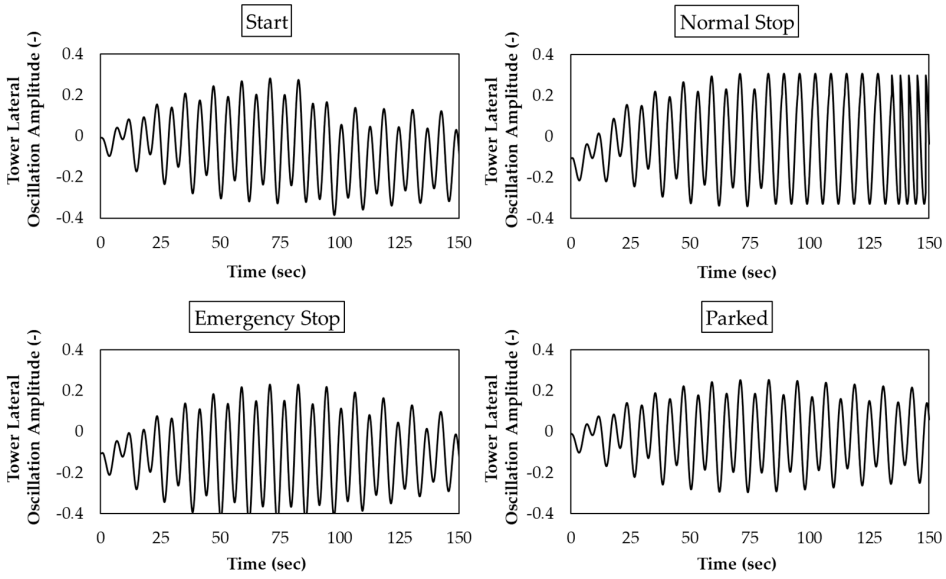


Figure 8. Tower's lateral oscillation amplitude for different phases of operation.

During the start phase, the oscillation amplitude gradually increases as the rotor accelerates, reaching a stable oscillation pattern around ± 0.4. This phase demonstrates a

dynamic transition where the turbine experiences an increasing aerodynamic load as the blades pitch toward their optimal position.

In the normal stop phase, the oscillations show a steady decay as the rotor gradually slows down, reflecting controlled deceleration and reduced aerodynamic forces. This phase exhibits smoother damping compared to emergency stop, emphasizing a less abrupt load transition.

The emergency stop phase shows the most abrupt oscillation patterns. Initially, the amplitude spikes due to rapid deceleration triggered by overspeed conditions, followed by a relatively higher damping rate. This abrupt response highlights the structural stresses introduced during emergency braking, critical for evaluating transient load effects.

Finally, in the parked phase, oscillations stabilize at a low amplitude of around ± 0.2, indicating minimal aerodynamic excitation. The fully feathered blades and engaged shaft brake result in reduced lateral forces, maintaining the tower's stability under stationary conditions.

This comparative analysis reveals how different operational phases influence the tower's dynamic behavior, providing valuable insights into transient load effects and structural stability under varying scenarios.

3.2. Force and Moment

Figure 9 presents the lateral (Fy) forces acting on the monopile at the mud-line for the four operational phases: start, normal stop, emergency stop, and parked. These force variations reflect the influence of aerodynamic and hydrodynamic loading during different operational transitions.

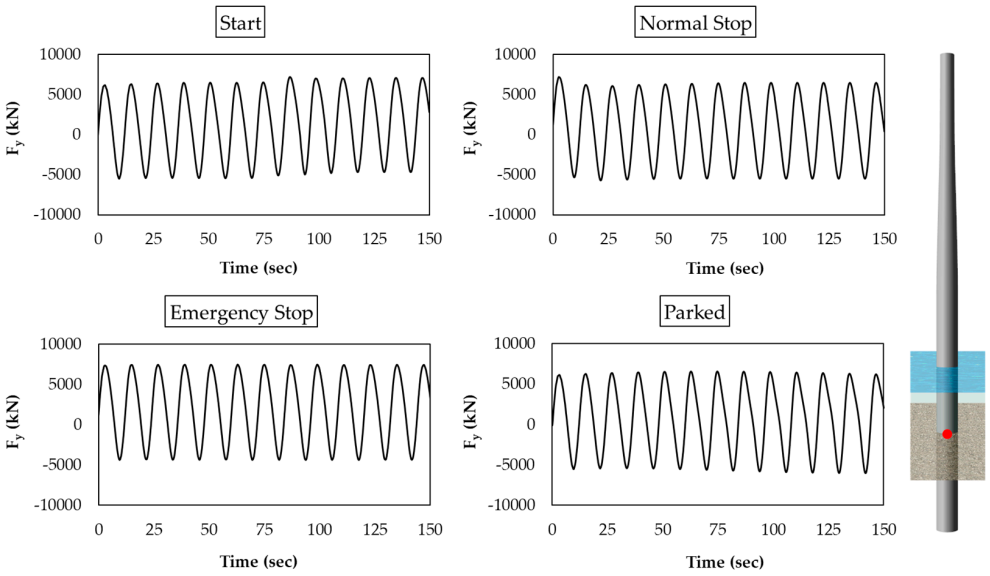


Figure 9. Lateral (Fy) force on monopile at mud-line (red dot shows the exact location).

Figure 10 shows that during the start phase, the lateral force oscillates significantly, increasing in amplitude as the turbine transitions from rest to full operation. The force reaches a peak magnitude of approximately $\pm 10{,}000$ kN, driven by the gradual increase in aerodynamic loads as rotor speed accelerates. The oscillatory pattern suggests a continuous interaction between aerodynamic forces and monopile structural response.

In the normal stop phase, the force oscillations exhibit a steady decline as the rotor slows down. The oscillation amplitudes decrease from $\pm 10{,}000$ kN to nearly ± 7500 kN over time, reflecting a smooth reduction in aerodynamic loading. This controlled

transition ensures that the structural stresses diminish progressively, avoiding sudden force variations.

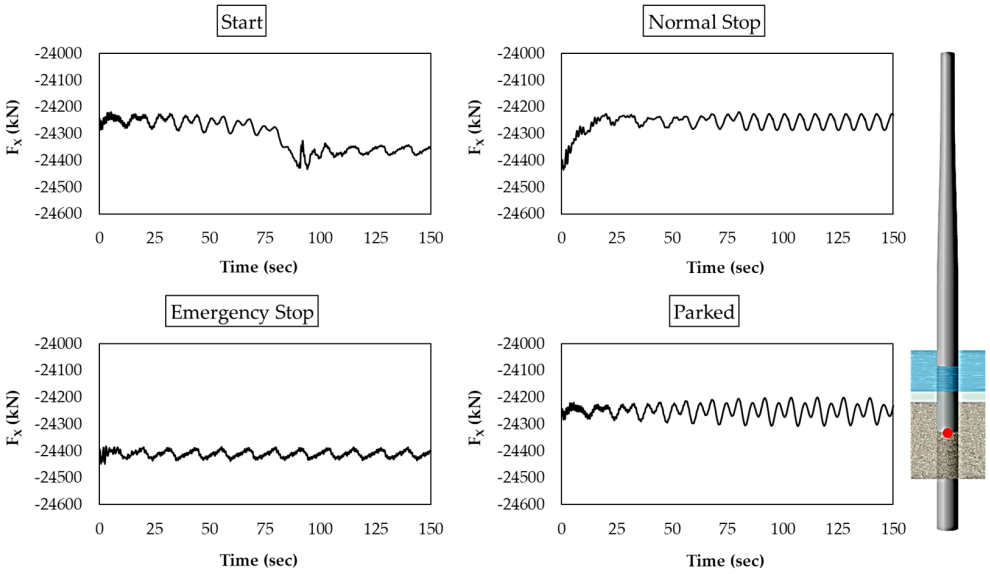


Figure 10. Lateral (Fx) force on monopile at mud-line (red dot shows the exact location).

The emergency stop phase experiences the most abrupt variations in lateral force. Initial force spikes, exceeding ±10,000 kN, occur due to rapid blade pitching and braking action. These forces dampen more rapidly than in the normal stop phase, indicating a sharper dynamic response under emergency conditions. The high oscillation frequency suggests an immediate structural adjustment to the sudden aerodynamic unloading. During the emergency stop phase, severe oscillations are observed due to the rapid aerodynamic unloading caused by sudden blade feathering and braking action. The abrupt transition from full operational load to minimal aerodynamic force results in a sudden redistribution of forces, generating high-frequency oscillations in lateral forces and moments. Additionally, structural inertial effects contribute to these oscillations as the monopile and tower system attempt to dissipate the residual kinetic energy accumulated before shutdown. The dynamic response is further amplified by aerodynamic damping reductions, as the absence of steady-state wind loads diminishes the stabilizing aerodynamic effects that are present during normal operation.

In the parked phase, the lateral forces stabilize at minimal oscillations near ±5000 kN. With fully feathered blades and a stationary rotor, aerodynamic loads are significantly reduced, ensuring the monopile remains in a relatively stable condition under the influence of hydrodynamic forces alone.

At the mud-line, the lateral forces exhibit a consistently high baseline across all phases due to the fixed constraints at the seabed and the monopile's structural stiffness. During the start phase, there is a gradual increase in oscillation superimposed on the baseline force, reflecting dynamic loading from wind and waves.

In the normal stop phase, the oscillations gradually diminish as the rotor slows down, indicating a smooth reduction in lateral loads. The baseline force remains nearly constant, emphasizing the monopile's structural constraints.

The emergency stop phase shows sharp oscillations at the onset, reflecting abrupt aerodynamic and hydrodynamic load variations. However, these oscillations dampen rapidly, stabilizing near the baseline force, similar to the normal stop phase but with higher initial intensity.

In the parked phase, oscillations are minimal, and the lateral force remains steady at the baseline value, demonstrating structural stability under stationary conditions.

The key differences between phases are evident in the force magnitudes and damping rates. The emergency stop phase experiences the highest transient forces, emphasizing the need for a robust structural design to withstand abrupt load changes. The normal stop and parked phases show controlled and minimal loading, respectively, highlighting the influence of operational strategies on lateral force dynamics. The consistently higher baseline force reflects the monopile's anchoring constraints, critical for maintaining stability under varying conditions.

Figure 11 presents the lateral moments (My) acting on the monopile at the mud-line for the four operational phases: start, normal stop, emergency stop, and parked. These results highlight the variations in dynamic moments and structural behavior due to changes in operational and environmental loading conditions.

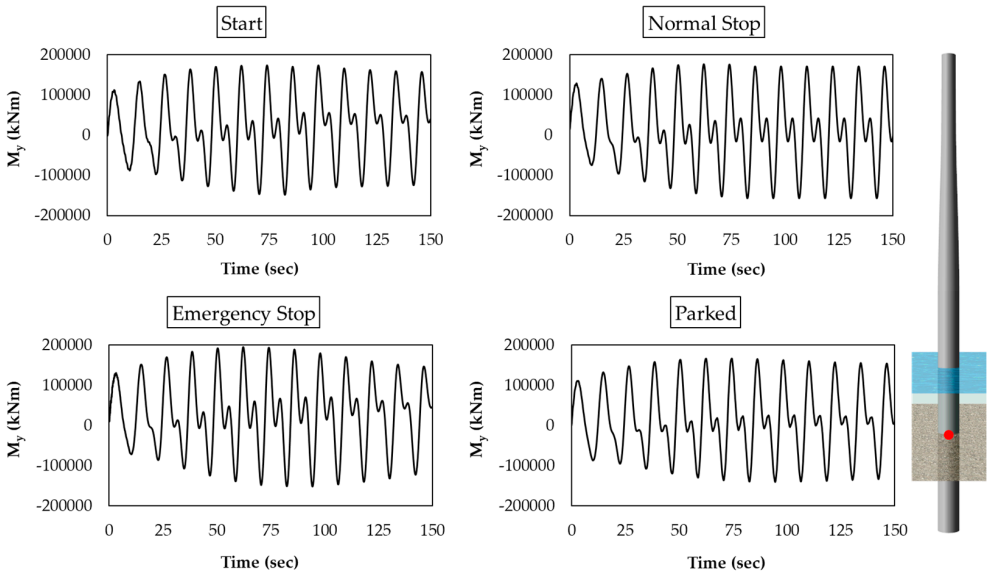


Figure 11. Lateral (My) moment on monopile at mud-line (red dot shows the exact location).

Figure 12 shows that during the start phase, the lateral moment exhibits a steady increase in oscillation amplitude as the rotor accelerates. Peak moment values reach approximately ±100,000 kNm, driven by the progressive aerodynamic loading as the blades pitch toward their optimal position. The oscillations become more pronounced after 75 s, indicating increasing structural excitation due to dynamic aerodynamic forces.

In the normal stop phase, the oscillation amplitudes decrease as the rotor decelerates. The moment transitions smoothly from ±100,000 kNm to around ±75,000 kNm, reflecting a controlled reduction in aerodynamic forces. This behavior ensures that transient stresses are gradually reduced, minimizing sudden structural disturbances.

The emergency stop phase exhibits the most abrupt moment variations, with high initial oscillations reaching approximately ±100,000 kNm. These rapid fluctuations result from the sudden aerodynamic unloading due to immediate blade feathering and shaft braking. The moment dampens at a faster rate than in the normal stop phase, but the initial intensity is notably higher, emphasizing the structural impact of emergency stopping conditions. The reported moments have been compared with reference peak bending values from the NREL IEA 15 MW wind turbine to assess structural safety margins. The observed peak moment in this study, reaching up to ±100,000 kNm during the emergency stop phase, falls within the expected range for large-scale offshore wind turbines. Specifically, the maximum tower base moments in the side–side and fore–aft directions exceed

400,000 kNm [49], indicating that the reported moments remain significantly lower than these extreme loading conditions. This comparison validates that the monopile operates within a safe margin, reinforcing the structural resilience of the design under transient loading conditions.

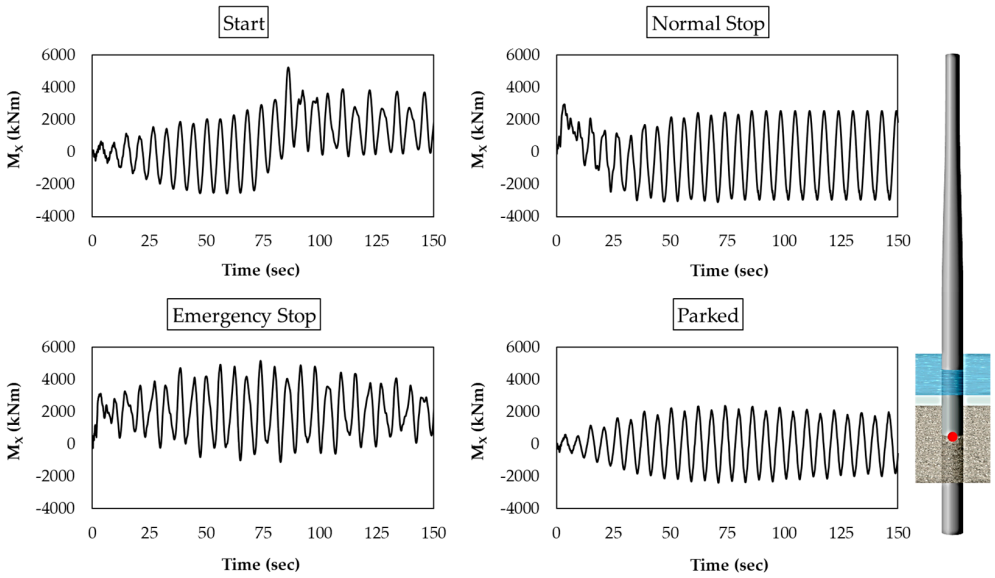


Figure 12. Lateral (Mx) moment on monopile at mud-line (red dot shows the exact location).

In the parked phase, the lateral moment stabilizes with minimal oscillations, remaining close to ±50,000 kNm. With the rotor fully stopped and blades in a feathered position, aerodynamic loading is significantly reduced, leaving only hydrodynamic forces influencing the monopile's structural response.

During the start phase, although the moments exhibit a steady increase in oscillation amplitude as the turbine begins operation, the magnitudes are very small due to the monopile's reduced leverage at the mud-line position.

In the normal stop phase, the moments decrease gradually. The controlled reduction in aerodynamic forces is evident, with oscillations dampening over time.

The emergency stop phase shows sharp initial oscillations, reflecting abrupt load variations. However, the moment magnitudes are lower, peaking at ±6000 kNm. The rapid damping highlights the structural stability of the monopile during emergency conditions.

The parked phase exhibits minimal oscillations, with lateral moments stabilizing at near-zero values. The stationary state ensures that dynamic loading is negligible at this location.

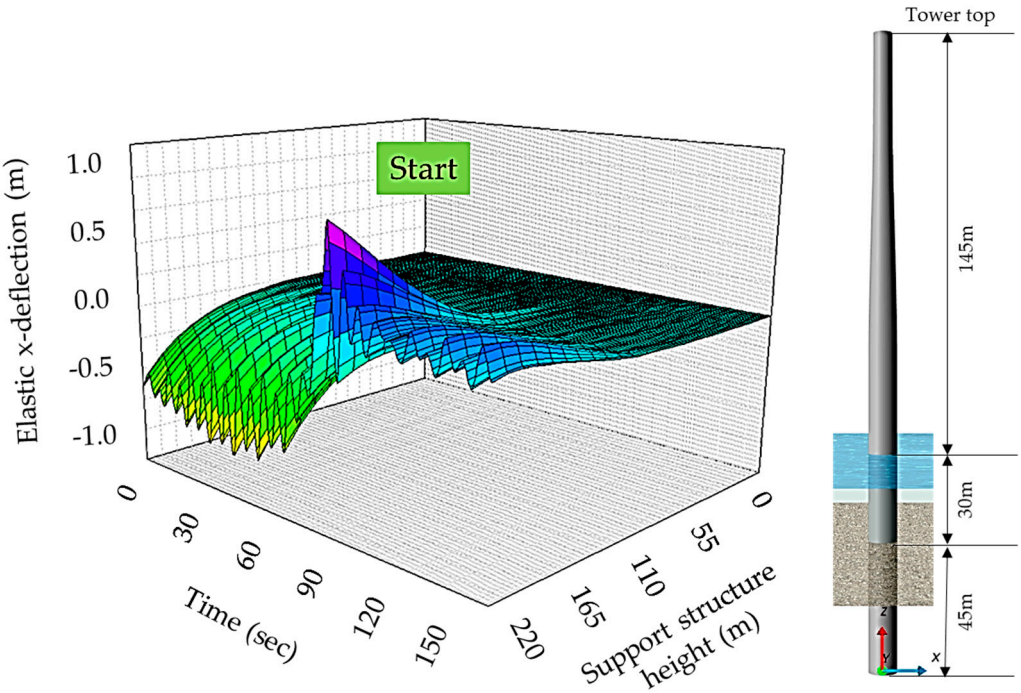
The lateral moments are significantly higher across all operational phases. This disparity is attributed to the monopile's structural geometry, where forces acting experience greater leverage. The emergency stop phase consistently shows the highest dynamic response at both locations, emphasizing the critical role of emergency braking in structural design. In contrast, the parked phase exhibits the lowest moments, ensuring structural stability under stationary conditions.

This comparative assessment provides key insights into the distribution of moments along the monopile, highlighting the need for a robust design to accommodate dynamic forces and moments during transient and extreme operational scenarios.

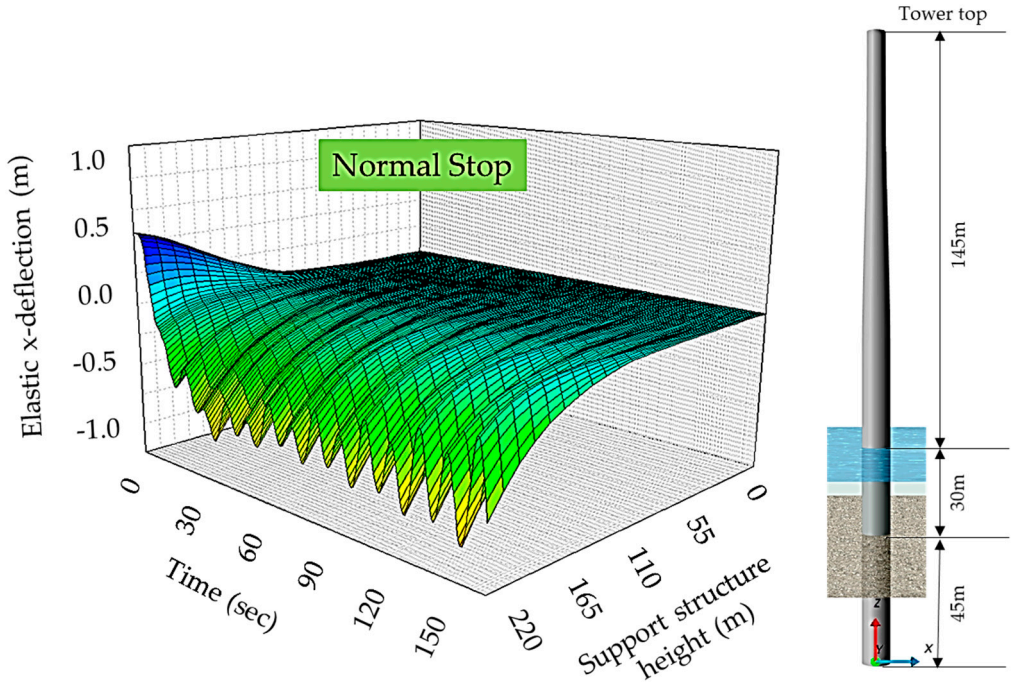
3.3. Elastic Deformation

Figure 13 presents the lateral deflection along the height of the monopile and tower in the x-direction for four operational phases: start, normal stop, emergency stop, and

parked. Each phase shows distinct deformation trends, reflecting the dynamic structural response under varying aerodynamic and operational conditions. The deflection patterns are analyzed technically and physically to understand their implications.

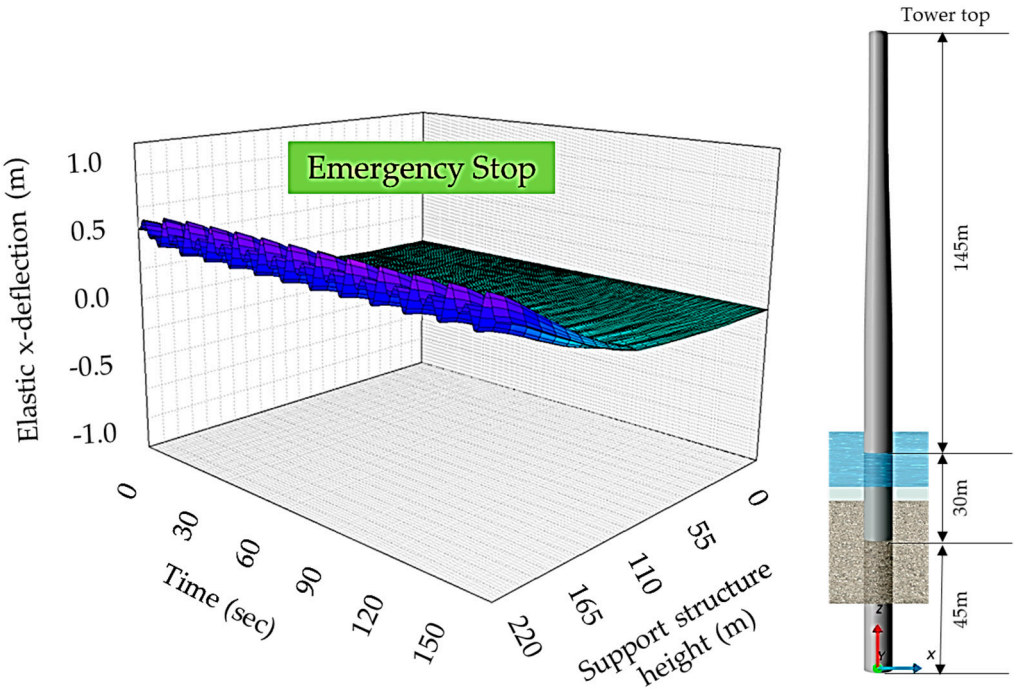


(**a**)

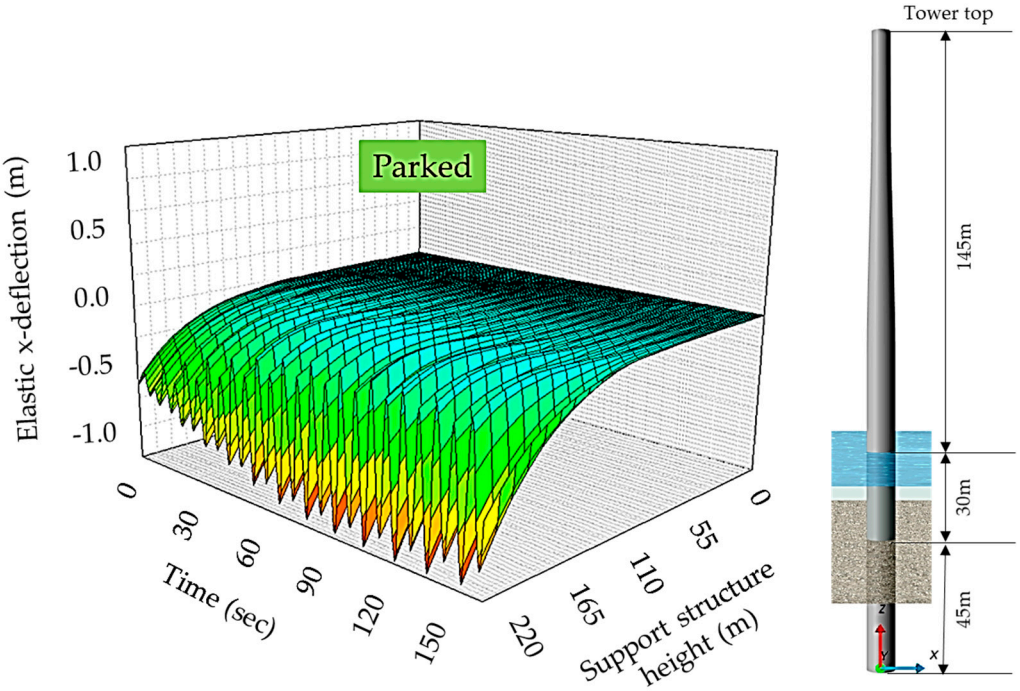


(**b**)

Figure 13. *Cont.*



(**c**)



(**d**)

Figure 13. Lateral (x-direction) deflection along the entire length of the tower and monopile with respect to time: (**a**) start; (**b**) normal stop; (**c**) emergency stop; (**d**) parked.

During the start phase, the deflection initially oscillates between −0.5 m and 0.5 m near the tower's mid-section, reflecting the dynamic aerodynamic loads as the rotor begins to accelerate. Around 90 s, a significant transition occurs where the deflection shifts abruptly from negative to positive, with the peak reaching approximately 1 m. The displacement direction reversal during the start phase occurs due to the progressive shift in aerodynamic force distribution as the rotor accelerates. Initially, the turbine is at rest with blades in a

feathered position, leading to minimal aerodynamic force. As the blades begin pitching toward the optimal power-generating angle, aerodynamic loads gradually increase, resulting in initial displacement in one direction. However, once the rotor achieves higher rotational speeds, the aerodynamic loading pattern undergoes a shift, leading to a reversal in displacement direction. This effect is further influenced by monopile flexibility and soil–structure interaction, which contribute to transient structural responses during the early stages of operation.

As mentioned above, a maximum lateral displacement of 1.0 m was observed at the tower's top during the start phase. To evaluate the acceptability of this displacement, a serviceability analysis was conducted in line with the principles outlined in DNVGL-OS-J101. This involved assessing the impact of the observed displacement on the structural performance and operational efficiency of the wind turbine. The analysis indicates that the 1.0 m displacement remains within acceptable limits, ensuring that the structural integrity and functionality of the turbine are maintained.

In the normal stop phase, the deflection exhibits a smooth transition from positive to negative during the first 30 s, stabilizing around -0.8 m for the remainder of the simulation. This behavior reflects the gradual reduction in aerodynamic forces as the rotor decelerates. The smooth transition from positive to negative indicates a steady unloading of the tower, with aerodynamic forces diminishing while hydrodynamic forces remain consistent. Scientifically, this highlights the importance of controlled deceleration in reducing structural oscillations and preventing abrupt load redistributions that could induce fatigue.

For the emergency stop phase, the deflection remains consistently positive throughout the simulation, with peak values reaching approximately 0.5 m near the top of the tower. This constant positive deflection is caused by the rapid pitching of the blades to their feathered position, which abruptly reduces aerodynamic loads but maintains a unidirectional force distribution. Physically, the lack of negative deflection indicates that aerodynamic unloading is dominant during this phase, while the structural system rapidly stabilizes. This highlights the monopile's robustness in responding to sudden operational interruptions without significant oscillations.

In the parked phase, the deflection is consistently negative, stabilizing around -0.7 m. The fully feathered blades and stationary rotor minimize aerodynamic loads, resulting in a near-constant hydrodynamic load as the primary force acting on the structure. This negative deflection represents the monopile's natural deformation under the combined effect of wave and current forces. Scientifically, this phase underscores the monopile's ability to maintain structural stability under static operational conditions.

The deflection trends across these phases reveal critical insights into the dynamic behavior of the monopile and tower. The abrupt transition in the start phase and the smooth oscillation reduction in the normal stop phase emphasize the structural system's adaptability under varying aerodynamic conditions. The consistent deflection in the emergency stop and parked phases highlights the monopile's stability under extreme and static conditions. These results provide valuable data for designing monopile support structures capable of enduring transient and static loading conditions while minimizing long-term fatigue and deformation risks.

3.4. Support Structure Rotational Deflection

Figure 14 illustrates the angular rotation about the x-axis on the monopile at the mud-line under four operational phases: start, normal stop, emergency stop, and parked. The results highlight the dynamic rotational behavior of the monopile under varying

aerodynamic and hydrodynamic forces, providing insights into its structural response during different phases of operation.

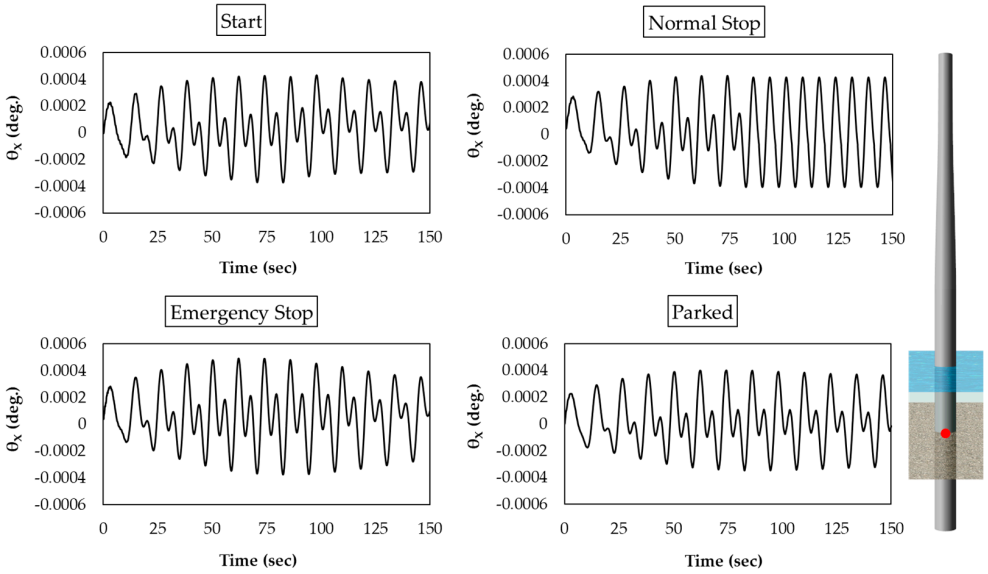


Figure 14. Angular rotation (about *x*-axis) on monopile at mud-line (red dot shows the exact location).

During the start phase, the angular rotation increases gradually, with oscillation amplitudes peaking at approximately ±0.0006 degrees after 90 s. This behavior corresponds to the increasing aerodynamic loads on the tower as the rotor accelerates, inducing greater structural excitation at the mud-line. The oscillation frequency remains steady throughout this phase, indicating a continuous buildup of aerodynamic forces.

In the normal stop phase, the rotational oscillations exhibit a smooth decay, stabilizing near ±0.0004 degrees. The gradual reduction in aerodynamic forces as the rotor slows down results in a controlled decrease in structural response. The damping effect prevents sudden rotational changes, reducing the risk of excessive monopile deformation.

The emergency stop phase shows rapid rotational oscillations, with peak values reaching approximately ±0.0005 degrees. These sharp oscillations are caused by abrupt aerodynamic and structural load changes due to the rapid blade pitch adjustment. The high-frequency response highlights the transient nature of emergency shutdown conditions, where sudden deceleration leads to an immediate structural reaction. However, the oscillation amplitude dampens relatively quickly, reflecting the monopile's ability to stabilize after the initial aerodynamic unloading.

In the parked phase, angular rotations remain minimal, oscillating consistently around ±0.0003 degrees. The absence of significant aerodynamic forces due to the fully feathered blades and stationary rotor results in a stable monopile condition. The structural response is primarily governed by hydrodynamic forces, which induce only minor oscillatory motion.

These findings emphasize the importance of analyzing rotational behavior at the mud-line, where structural deformations are directly influenced by dynamic loading conditions. Understanding these rotational responses helps in optimizing monopile designs to withstand transient forces while ensuring long-term stability under operational and extreme conditions. The amplitudes of angular displacement vary slightly due to variations in aerodynamic damping effects and transient loading conditions. While the parked and start conditions display relatively steady oscillation ranges, the emergency stop condition introduces higher momentary fluctuations due to the rapid braking effect, which results in transient aerodynamic forces that briefly amplify monopile rotation.

In Figure 15, the angular rotation at the mud-line shows a similar increasing trend during the start phase, peaking at ±0.0008 degrees.

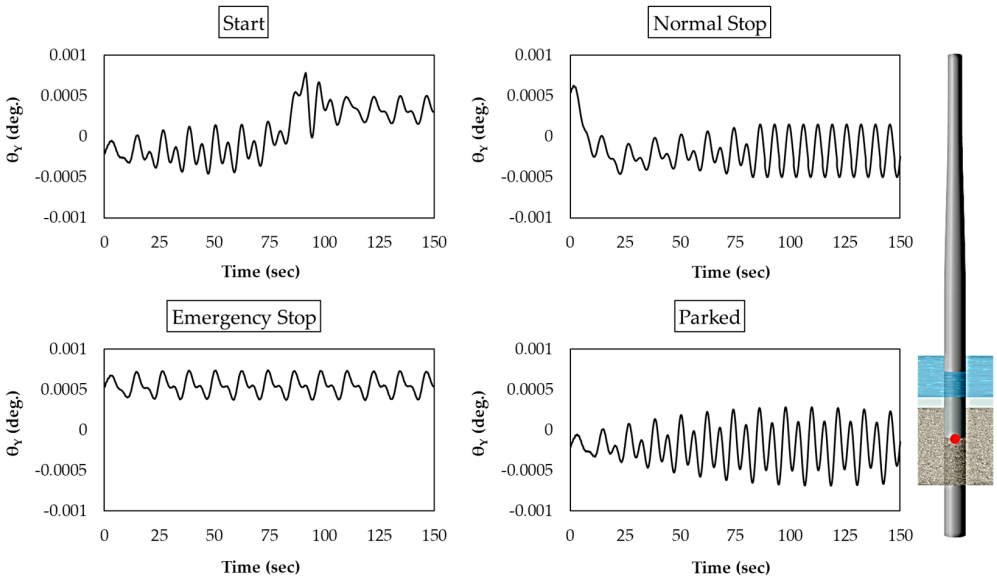


Figure 15. Angular rotation (about *y*-axis) on monopile at mud-line (red dot shows the exact location).

In the normal stop phase, the rotational oscillations decay steadily, with peak values stabilizing around ±0.0004 degrees. This reduced amplitude indicates less structural stress at the mud-line.

The emergency stop phase shows abrupt oscillations (but slightly dampened) with peaks around ±0.0007 degrees. The rapid stabilization reflects the effective load transfer along the monopile's height during sudden load changes.

In the parked phase, the angular rotation remains minimal at ±0.0002 degrees, reflecting the stationary condition and reduced dynamic loads acting at this location.

Across all phases, the start and emergency stop phases exhibit the highest rotational amplitudes, highlighting the structural challenges posed by transient and abrupt aerodynamic loading. The normal stop and parked phases demonstrate lower rotational amplitudes, emphasizing the effectiveness of controlled operations in reducing structural stress.

This comparative analysis underscores the importance of considering rotational dynamics at different monopile locations for robust structural design, particularly under transient and extreme operational conditions.

Lateral forces (Fx, Fy) directly contribute to moment generation (Mx, My) at the mud-line, which in turn influences angular displacement (θx, θy). During transient conditions, the monopile experiences fluctuating forces, leading to varying moment distributions along its height. These moments induce rotational displacements at the mud-line, with higher moment fluctuations corresponding to larger angular displacement variations.

3.5. Load Difference for Different Phases of Operations

Figure 16 illustrates the relative difference in lateral forces (Fx and Fy) between the parked condition and the other operational states: start, normal stop, and emergency stop. These differences highlight how the aerodynamic and hydrodynamic forces evolve during transitions between operational phases and their impact on the monopile's structural response.

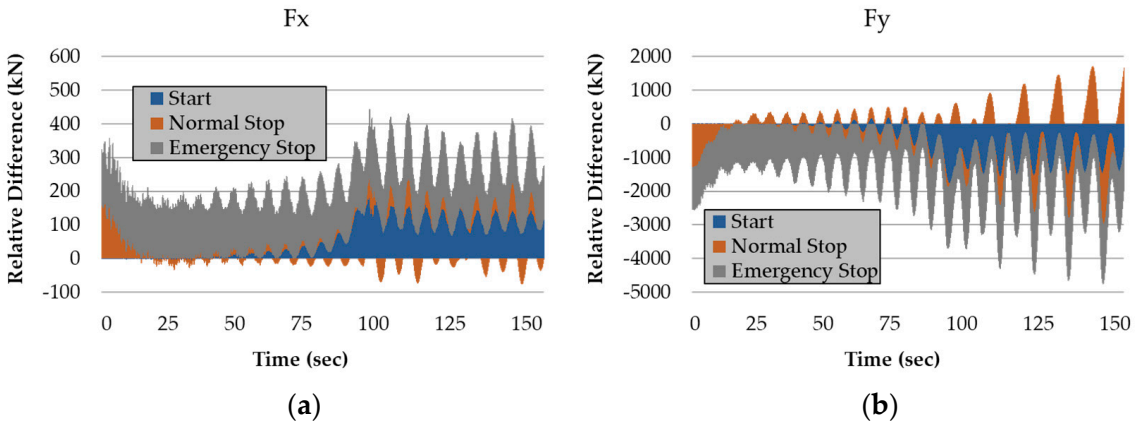


Figure 16. Lateral force relative difference between parked and other states of operation: (**a**) Fx; (**b**) Fy.

In Figure 16a, which presents the relative difference in Fx, a clear increasing trend is observed during the start phase. Initially, the force deviation remains close to 0 kN for the first 10 s, indicating negligible aerodynamic force changes. As the turbine accelerates, the force difference gradually increases, reaching approximately +50 kN at 75 s and fluctuating within a range of +70 kN to +180 kN toward the end of the simulation at 150 s. This steady increase reflects the rising aerodynamic forces as the rotor gains speed, leading to higher lateral loading on the monopile. In the normal stop phase, the force difference remains relatively small in the early stages, gradually increasing after 25 s and reaching around +50 kN at 75 s. Unlike the start phase, where force differences continue to grow, the normal stop phase shows a more controlled reduction in aerodynamic forces, with oscillations normally stabilizing within −70 kN to +210 kN after 100 s. This behavior indicates that gradual rotor deceleration prevents excessive force redistributions, reducing structural stress during stopping operations. The emergency stop phase exhibits the most abrupt variations, with sharp force oscillations reaching between +150 kN and +350 kN within the first 50 s. These fluctuations reflect the sudden aerodynamic unloading due to rapid blade pitch adjustments and shaft braking. After 100 s, the force stabilizes in the range of +200 kN to +450 kN, though high-frequency oscillations persist. The significant transient forces observed in this phase highlight the structural challenges associated with emergency stopping conditions.

Figure 16b presents the relative difference in Fy, further capturing the aerodynamic response of the turbine and its effect on the monopile's lateral loading. During the start phase, the force initially remains stable but gradually increases, reaching approximately −100 kN at 50 s. This indicates the increasing influence of aerodynamic forces as the turbine transitions to full operational speed. After 100 s, the oscillations become more regular, fluctuating around −2000 kN, showing the sustained aerodynamic load increase as the turbine reaches a stable power production state. The normal stop phase exhibits a smoother force transition compared to the start phase, with the force difference gradually shifting from −500 kN to +500 kN over the first 75 s, after which it stabilizes within −3000 kN to +1500 kN. The reduced fluctuation range suggests a controlled aerodynamic force decrease, minimizing structural load variations during normal stopping procedures. The emergency stop phase shows the most extreme force fluctuations, with the relative difference varying sharply between −2000 kN and −2500 kN within the first 75 s. These abrupt variations correspond to rapid aerodynamic force redistributions due to immediate blade feathering and braking. After 100 s, the force stabilizes, but oscillations remain significant, indicating that emergency stopping introduces the most dynamic loading on the monopile.

Figure 17 presents the relative difference in moments (Mx and My) between the parked condition and other operational phases, including start, normal stop, and emergency stop.

These differences highlight the varying structural responses of the monopile under transient aerodynamic and hydrodynamic loading conditions.

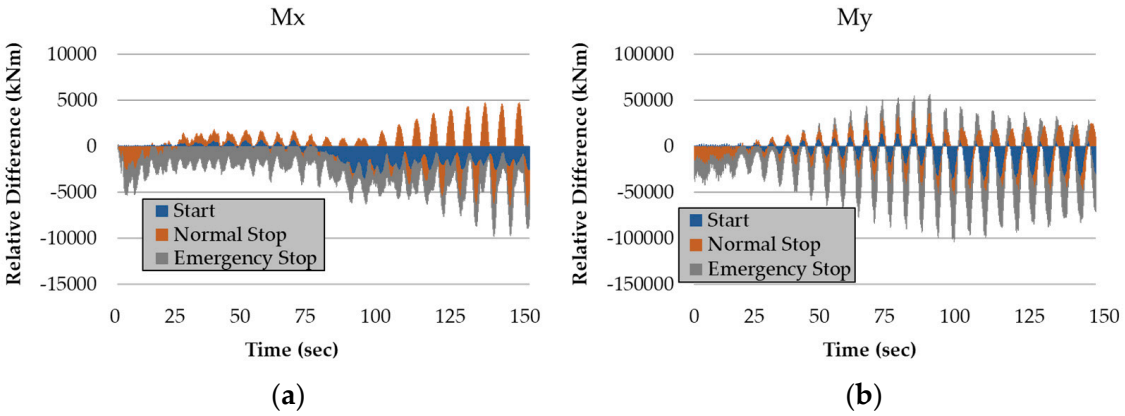


Figure 17. Moment relative difference between parked and other states of operation: (**a**) Mx; (**b**) My.

In Figure 17a, the relative difference in Mx illustrates a gradual increase in deviation as the turbine transitions through different phases. During the start phase, the moment difference remains relatively small in the initial 25 s, staying close to 0 kNm, indicating minimal structural change from the parked condition. As the turbine accelerates, the relative moment difference gradually increases, reaching approximately ±500 kNm at 75 s, followed by sustained oscillations in the range of −2000 kNm to −3000 kNm after 100 s. The increasing oscillation amplitude reflects the monopile's response to rising aerodynamic forces as the rotor reaches operational speeds. In the normal stop phase, the moment difference follows a smoother transition, increasing steadily and stabilizing around ±4000 kNm after 100 s. This behavior suggests a controlled reduction in aerodynamic loading as the rotor slows down, preventing excessive structural stress variations. The emergency stop phase exhibits the most pronounced oscillatory behavior, with large moment variations reaching up to −5000 kNm in the first 50 s due to rapid aerodynamic unloading from blade pitching and braking. The oscillation amplitude remains significantly higher than in other phases, with fluctuations between −5000 kNm and −10,000 kNm persisting throughout the simulation. These sharp variations indicate that emergency stopping introduces substantial dynamic moments, requiring careful structural design considerations.

Figure 17b shows the relative difference in My, which follows a more extreme variation pattern than Mx due to the increased aerodynamic and hydrodynamic coupling effects in this direction. During the start phase, the moment difference gradually increases from 0 kNm and reaches approximately ±10,000 kNm at 75 s. The oscillations become more prominent as the turbine reaches full operational speed, stabilizing around ±40,000 kNm after 100 s, demonstrating the significant impact of aerodynamic forces in this direction. In the normal stop phase, the moment difference increases steadily and stabilizes around ±40,000 kNm after 100 s, showing a controlled transition as the rotor decelerates. The emergency stop phase again exhibits the most extreme variations, with moment differences initially oscillating around ±60,000 kNm within the first 50 s due to abrupt aerodynamic unloading. After 100 s, the oscillation amplitude remains high, fluctuating between ±50,000 kNm and ±100,000 kNm, emphasizing the structural challenges posed by emergency shutdown conditions.

Figure 18 presents the relative difference in angular displacement (θx and θy) between the parked condition and the other operational states: start, normal stop, and emergency stop. These differences highlight how rotational deflections evolve under varying aero-

dynamic and hydrodynamic loading conditions, affecting the monopile's stability during different operational phases.

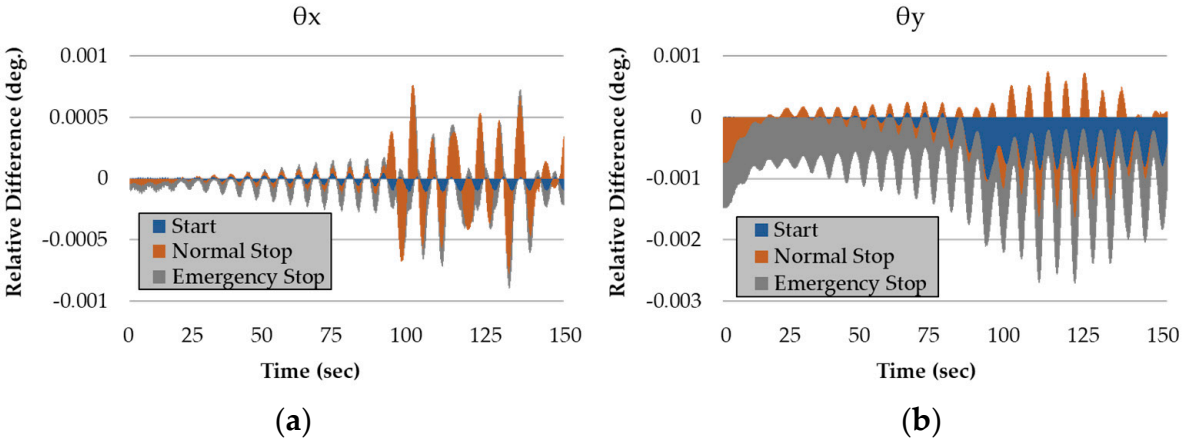


Figure 18. Angular displacement relative difference between parked and other states of operation: (**a**) θx; (**b**) θy.

In Figure 18a, which shows the relative difference in angular displacement about the *x*-axis (θx), the start phase exhibits a gradual increase in oscillations, beginning near 0 degrees and reaching approximately ±0.0001 degrees at 75 s. The oscillations intensify as the turbine reaches full operational speed, stabilizing between ±0.0002 degrees and ±0.0003 degrees after 100 s. This increasing rotational deviation suggests that aerodynamic forces generate significant bending effects along the *x*-axis as the rotor accelerates. In the normal stop phase, the angular displacement follows a controlled reduction, with oscillations peaking around ±0.0002 degrees before stabilizing at approximately ±0.0008 degrees after 100 s. The smoother variation compared to the start phase indicates a gradual unloading of aerodynamic forces, minimizing structural disturbances. The emergency stop phase exhibits the most pronounced variations, with high-frequency oscillations reaching −0.0002 degrees in the first 50 s, due to the sudden aerodynamic unloading from rapid blade feathering and braking. The oscillation amplitudes remain high throughout the simulation, with deviations fluctuating between ±0.0002 degrees and ±0.0009 degrees, emphasizing the monopile's dynamic response to emergency shutdown conditions.

In Figure 18b, which presents the relative difference in angular displacement about the *y*-axis (θy), the trends are more extreme, reflecting stronger lateral bending effects. During the start phase, the angular displacement initially remains close to 0 degrees but increases steadily, reaching approximately −0.0005 degrees at 50 s. The oscillations continue to grow, stabilizing between −0.0007 degrees and −0.001 degrees after 100 s. This pattern highlights the increasing aerodynamic-induced rotation about the *y*-axis as the turbine gains speed. The normal stop phase follows a similar trend but with more controlled oscillations, transitioning from −0.005 degrees to +0.005 degrees over the first 75 s and stabilizing within −0.0015 degrees to +0.001 degrees. This behavior indicates a smoother aerodynamic force reduction compared to the start phase, reducing rotational stress on the monopile. The emergency stop phase, however, displays the most extreme oscillations, with angular displacement fluctuating between −0.0015 degrees and +0.0005 degrees in the first 75 s due to abrupt aerodynamic unloading. Even after 100 s, oscillations remain significant, varying between −0.0022 degrees and −0.0027 degrees, indicating the structural challenges posed by emergency braking.

4. Discussion and Future Recommendations

The dynamic structural analysis of the monopile support structure for the 15 MW offshore wind turbine highlights critical differences in structural behavior under transient loading conditions across various operational phases: start, normal stop, emergency stop, and parked. The results provide a comprehensive understanding of the interplay between aerodynamic, hydrodynamic, and structural forces, leading to several key findings. During the start phase, a sudden shift in deflection was observed, with a pronounced transition from negative to positive values at approximately 90 s. This phenomenon reflects the changing aerodynamic force distribution as the turbine transitions to full operation. In contrast, the normal stop phase demonstrated a smooth reduction in loads, underscoring the importance of controlled deceleration for minimizing transient stresses. The emergency stop phase showed abrupt changes in loads and deflections, emphasizing the structural challenges during rapid shutdowns, while the parked phase indicated stable structural behavior under static conditions.

The force and moment distribution further revealed that the monopile consistently experienced very high forces and moments at the mud-line. The emergency stop phase showed the highest transient forces and moments, highlighting the need for robust designs to withstand sudden load changes. The parked phase, on the other hand, displayed minimal dynamic forces, indicating structural stability during stationary periods. Transient phases such as start and emergency stop exhibited higher rotational amplitudes, whereas normal stop and parked phases showed reduced rotation, ensuring long-term stability. The elastic deformation trends provided valuable insights into structural stability and stress distribution. The consistently positive deflection during the emergency stop phase and consistently negative deflection during the parked phase highlight the distinct force regimes under dynamic and static conditions, respectively.

To further enhance the understanding and applicability of monopile support structures for offshore wind turbines, several future directions are proposed. Improved material modeling is recommended to incorporate advanced materials with higher fatigue resistance and load-bearing capacity to address the challenges posed by extreme transient loads, particularly during emergency stop conditions. Extending the simulation scenarios to include additional operational cases such as extreme weather events, yaw misalignment, and tidal forces would provide a more comprehensive range of loading conditions and their impact on structural performance. Additionally, integrating soil–structure interaction effects into the analysis can capture the variability in seabed conditions and their influence on load distribution, particularly during transient phases.

The optimization of structural design using multi-objective optimization frameworks is suggested to minimize structural deflection and rotational amplitudes while ensuring economic viability, especially for ultra-large turbines like the 15 MW model. Experimental validation through scaled physical experiments in wave tanks and wind tunnels is critical for refining numerical simulations and improving reliability. Lastly, assessing the environmental impact of monopile dynamics, particularly in terms of vibration transmission to the seabed, is essential to develop mitigation strategies that minimize ecological disturbance.

While this study primarily focused on transient structural behavior during different operational phases, fatigue analysis remains a critical aspect of offshore wind turbine monopile performance, particularly under cyclic aerodynamic and hydrodynamic loads. During transient conditions, abrupt variations in force and moment distributions contribute to increased stress fluctuations, potentially accelerating fatigue damage accumulation. In particular, the emergency stop phase exhibited the most extreme moment oscillations ($\pm$100,000 kNm), which could significantly influence fatigue life by introducing high-amplitude, short-duration stress cycles. Future research should integrate comprehensive

fatigue life assessments using load spectrum analysis and S-N curve methodologies to quantify the long-term structural integrity of monopile-supported offshore wind turbines. The application of Palmgren–Miner cumulative fatigue models will allow for accurate estimation of fatigue damage ratios, ensuring optimized support structure designs for enhanced durability. Additionally, the incorporation of site-specific material fatigue properties, including composite and structural steel, will further refine fatigue predictions and guide material selection for long-term offshore wind applications.

By addressing these recommendations, the design and analysis of monopile support structures can be further refined, contributing to the development of safer, more efficient, and sustainable offshore wind energy systems.

5. Conclusions

This study conducted a comprehensive transient analysis of the dynamic structural response of a 15 MW offshore wind turbine monopile at the mud-line, evaluating lateral forces, moments, and angular displacements across four operational phases. The start phase exhibited a gradual force and moment buildup, with Fx reaching +180 kN, Fy stabilizing at -2000 kN, Mx fluctuating between -2000 and -3000 kNm, and My oscillating up to $\pm$140,000 kNm. The normal stop phase showed a smoother force and moment decay, with oscillations stabilizing at $\pm$4000 kNm for Mx and $\pm$100,000 kNm for My, while force differences ranged from -3000 kN to +1500 kN. The emergency stop phase demonstrated the most extreme structural variations, with Fx peaking at +450 kN, Fy fluctuating between -2000 and -2500 kN, Mx reaching -5000 kNm, and My exhibiting high-amplitude oscillations between $\pm$50,000 kNm and $\pm$100,000 kNm. These variations underscore the significant aerodynamic unloading effects during emergency shutdowns, highlighting the need for structural reinforcements to manage transient load variations effectively.

Angular displacement analysis highlighted critical rotational deviations under transient conditions. The start phase exhibited θx stabilizing at $\pm$0.0003 degrees and θy at -0.001 degrees, while the normal stop phase showed a controlled reduction, with θx stabilizing at $\pm$0.0008 degrees and θy between -0.0015 and +0.001 degrees. The emergency stop phase induced the largest angular fluctuations, with θx oscillating up to $\pm$0.0009 degrees and θy ranging from -0.0022 to -0.0027 degrees. These findings emphasize the importance of improving damping mechanisms and optimizing monopile design to mitigate transient aerodynamic and hydrodynamic loads effectively. While this study focuses on short-term transient behavior, future work will explore fatigue life assessment to evaluate the long-term performance and durability of monopile-supported offshore wind turbines. These insights contribute to enhancing structural reliability, improving load mitigation strategies, and ensuring safer and more resilient offshore wind turbine support structures.

Author Contributions: Conceptualization, S.A. and D.L.; methodology, S.A.; software, S.A.; validation, S.A. and M.W.; formal analysis, S.A.; investigation, S.A.; resources, S.A.; data curation, D.L.; writing—original draft preparation, S.A.; writing—review and editing, D.L.; visualization, M.W.; supervision, D.L.; project administration, D.L.; funding acquisition, D.L. All authors have read and agreed to the published version of the manuscript.

Funding: This work was supported by the Human Resources Development of the Korea Institute of Energy Technology Evaluation and Planning (KETEP) grant funded by the Korean government's Ministry of Trade, Industry and Energy (No. RS-2021-KP002506). This work was supported by the Korea Institute of Energy Technology Evaluation and Planning (KETEP) grant funded by the Korean government (MOTIE) (20224000000220, Jeonbuk Regional Energy Cluster Training of Human Resources).

Institutional Review Board Statement: Not applicable.

Informed Consent Statement: Not applicable.

Data Availability Statement: The data presented in this study are available on request from the corresponding author.

Acknowledgments: The authors would like to express their gratitude to KMA for providing the wind and wave data sets.

Conflicts of Interest: The authors declare no conflicts of interest.

References

1. *IEC 61400-1*; Wind Turbine Generator Systems—Part 1: Safety Requirements. IE Commission: Geneva, Switzerland, 1999.
2. Katsanos, E.I.; Thöns, S.; Georgakis, C.T. Wind turbines and seismic hazard: A state-of-the-art review. *Wind Energy* **2016**, *19*, 2113–2133. [CrossRef]
3. Asareh, M.-A.; Schonberg, W.; Volz, J. Effects of seismic and aerodynamic load interaction on structural dynamic response of multi-megawatt utility scale horizontal axis wind turbines. *Renew. Energy* **2016**, *86*, 49–58. [CrossRef]
4. Katsanos, E.I.; Sanz, A.A.; Georgakis, C.T.; Thöns, S. Multi-hazard response analysis of a 5MW offshore wind turbine. *Procedia Eng.* **2017**, *199*, 3206–3211. [CrossRef]
5. Yang, Y.; Ye, K.; Li, C.; Michailides, C.; Zhang, W. Dynamic behavior of wind turbines influenced by aerodynamic damping and earthquake intensity. *Wind Energy* **2018**, *21*, 303–319. [CrossRef]
6. Santangelo, F.; Failla, G.; Santini, A.; Arena, F. Time-domain uncoupled analyses for seismic assessment of land-based wind turbines. *Eng. Struct.* **2016**, *123*, 275–299. [CrossRef]
7. Avossa, A.M.; Demartino, C.; Ricciardelli, F. Assessment of the peak response of a 5MW HAWT under combined wind and seismic induced loads. *Open Constr. Build. Technol. J.* **2017**, *11*, 441–457. [CrossRef]
8. Mo, R.; Kang, H.; Li, M.; Zhao, X. Seismic fragility analysis of monopile offshore wind turbines under different operational conditions. *Energies* **2017**, *10*, 1037. [CrossRef]
9. Santangelo, F.; Failla, G.; Arena, F.; Ruzzo, C. On time-domain uncoupled analyses for offshore wind turbines under seismic loads. *Bull. Earthq. Eng.* **2018**, *16*, 1007–1040. [CrossRef]
10. Failla, G.; Santangelo, F.; Foti, G.; Scali, F.; Arena, F. Response-spectrum uncoupled analyses for seismic assessment of offshore wind turbines. *J. Mar. Sci. Eng.* **2018**, *6*, 85. [CrossRef]
11. Zuo, H.; Bi, K.; Hao, H. Dynamic analyses of operating offshore wind turbines including soil-structure interaction. *Eng. Struct.* **2018**, *157*, 42–62. [CrossRef]
12. Wang, P.; Zhao, M.; Du, X.; Liu, J.; Xu, C. Wind, wave and earthquake responses of offshore wind turbine on monopile foundation in clay. *Soil Dyn. Earthq. Eng.* **2018**, *113*, 47–57. [CrossRef]
13. Ju, S.-H.; Huang, Y.-C. Analyses of offshore wind turbine structures with soil-structure interaction under earthquakes. *Ocean Eng.* **2019**, *187*, 106190. [CrossRef]
14. Fan, J.; Li, Q.; Zhang, Y. Collapse analysis of wind turbine tower under the coupled effects of wind and near-field earthquake. *Wind Energy* **2019**, *22*, 407–419. [CrossRef]
15. Zuo, H.; Bi, K.; Hao, H.; Li, C. Influence of earthquake ground motion modelling on the dynamic responses of offshore wind turbines. *Soil Dyn. Earthq. Eng.* **2019**, *121*, 151–167. [CrossRef]
16. De Risi, R.; Bhattacharya, S.; Goda, K. Seismic performance assessment of monopile-supported offshore wind turbines using unscaled natural earthquake records. *Soil Dyn. Earthq. Eng.* **2018**, *109*, 154–172. [CrossRef]
17. Kaynia, A.M. Seismic considerations in design of offshore wind turbines. *Soil Dyn. Earthq. Eng.* **2019**, *124*, 399–407. [CrossRef]
18. Martín Del Campo, J.O.; Pozos-Estrada, A. Multi-hazard fragility analysis for a wind turbine support structure: An ap-plication to the Southwest of Mexico. *Eng. Struct.* **2020**, *209*, 109929. [CrossRef]
19. Kitahara, M.; Ishihara, T. Prediction of seismic loadings on wind turbine support structures by response spectrum method considering equivalent modal damping of support structures and reliability level. *Wind Energy* **2020**, *23*, 1422–1443. [CrossRef]
20. Wang, L.; Ishihara, T. A study of the effects of foundation uplift on the seismic loading of wind turbine tower and shallow foundation using a new dynamic Winkler model. *Eng. Struct.* **2020**, *219*, 110745. [CrossRef]
21. Witcher, D. Seismic analysis of wind turbines in the time domain. *Wind Energy Int. J. Prog. Appl. Wind Power Convers. Technol.* **2005**, *8*, 81–91. [CrossRef]
22. Bossanyi, E.A. *BLADED for Windows User Manual*; Garrad Hassan and Partners: Bristol, UK, 2000; p. 405.
23. Jonkman, J.M. *FAST User's Guide*; National Renewable Energy Laboratory Technical Report; National Renewable Energy Laboratory: Denver, CO, USA, 2005.
24. Henriksen, L.C.; Tibaldi, C.; Bergami, L. *HAWCStab2 User Manual*; Technical report; DTU Wind Energy (EN): Roskilde, Denmark, 2015.
25. Barter, G.E.; Sethuraman, L.; Bortolotti, P.; Keller, J.; Torrey, D.A. Beyond 15 MW: A cost of energy perspective on the next generation of drivetrain technologies for offshore wind turbines. *Appl. Energy* **2023**, *344*, 121272. [CrossRef]

26. Zhang, Y.; Song, Y.; Shen, C.; Chen, N.-Z. Aerodynamic and structural analysis for blades of a 15MW floating offshore wind turbine. *Ocean Eng.* **2023**, *287*, 115785. [CrossRef]
27. Chen, M.; Jiang, J.; Zhang, W.; Li, C.B.; Zhou, H.; Jiang, Y.; Sun, X. Study on mooring design of 15 MW floating wind turbines in South China Sea. *J. Mar. Sci. Eng.* **2023**, *12*, 33. [CrossRef]
28. Liu, J.; Xiao, Z.; Wang, K.; Huang, S.; Du, Y. Comparative study on dynamic responses of integrated installation process of a 5-MW and a 15-MW offshore wind turbine considering a pre-installed foundation. *Ocean Eng.* **2024**, *299*, 117399. [CrossRef]
29. Cao, J.; Qin, Z.; Ju, Y.; Chen, Y.; Shen, W.Z.; Shen, X.; Ke, S. Study of air compressibility effects on the aerodynamic performance of the IEA-15 MW offshore wind turbine. *Energy Convers. Manag.* **2023**, *282*, 116883. [CrossRef]
30. Pollini, N.; Pegalajar-Jurado, A.; Bredmose, H. Design optimization of a TetraSpar-type floater and tower for the IEA Wind 15 MW reference wind turbine. *Mar. Struct.* **2023**, *90*, 103437. [CrossRef]
31. Donnelly, O.; Anderson, F.; Carroll, J. Operations and Maintenance Cost Comparison Between 15 MW Direct-Drive and Medium-Speed Offshore Wind Turbines. *Wind Energy Sci. Discuss.* **2023**, *9*, 1345–1362. [CrossRef]
32. Trigaux, F.; Chatelain, P.; Winckelmans, G. Investigation of blade flexibility effects on the loads and wake of a 15 MW wind turbine using a flexible actuator line method. *Wind Energy Sci.* **2024**, *9*, 1765–1789. [CrossRef]
33. Zhu, Y.; Zhong, J.; Zhu, Y.; Chen, H.; Yu, X.; Chen, D. Effects of the yaw error and the fault conditions on the dynamic characteristics of the 15 MW offshore semi-submersible wind turbine. *Ocean Eng.* **2024**, *300*, 117440. [CrossRef]
34. Wang, J.; Ren, Y.; Shi, W.; Collu, M.; Venugopal, V.; Li, X. Multi-objective optimization design for a 15 MW semisubmersible floating offshore wind turbine using evolutionary algorithm. *Appl. Energy* **2024**, *377*, 124533. [CrossRef]
35. Fontanella, A.; Facchinetti, A.; Daka, E.; Belloli, M. Modeling the coupled aero-hydro-servo-dynamic response of 15 MW floating wind turbines with wind tunnel hardware in the loop. *Renew. Energy* **2023**, *219*, 119442. [CrossRef]
36. Russell, A.J.; Collu, M.; McDonald, A.S.; Thies, P.R.; Keane, A.; Quayle, A.R. LIDAR-assisted feedforward individual pitch control of a 15 MW floating offshore wind turbine. *Wind Energy* **2024**, *27*, 341–362. [CrossRef]
37. Lara, M.; Vázquez, F.; van Wingerden, J.-W.; Mulders, S.P.; Garrido, J. Multi-objective optimization of individual pitch control for blade fatigue load reductions for a 15 MW wind turbine. In Proceedings of the 2024 European Control Conference (ECC), Stockholm, Sweden, 25–28 June 2024; IEEE: Piscataway, NJ, USA, 2024; pp. 669–674.
38. Zhou, Z.; Chen, C.; Shen, X.; Zhou, X.; Hua, X. Conceptual design of a prestressed precast UHPC-steel hybrid tower to support a 15 MW offshore wind turbine. *Eng. Struct.* **2024**, *321*, 118939. [CrossRef]
39. Niranjan, R.; Ramisetti, S.B. Dynamic Response of 15 MW Floating Wind Turbine with Non-Redundant and Redundant Mooring Systems under Extreme and Accidental Conditions. *J. Offshore Mech. Arct. Eng.* **2023**, *145*, 062002. [CrossRef]
40. Gu, X.; Lin, F.; Jiang, W.; Xu, J.; Liu, J.-M.; Wang, K.; Tao, T. Power performance and dynamic characteristics of a 15 MW floating wind turbine with wave energy converter combined concept. *Sustain. Horiz.* **2025**, *13*, 100125. [CrossRef]
41. Chuang, Z.; Xia, L.; Qu, Y.; Li, W.; Li, J. Investigation of Structural Nonlinearity Effects on the Aero-elastic and Wake Characteristics of a 15 MW Wind Turbine. *J. Mar. Sci. Eng.* **2025**, *13*, 116. [CrossRef]
42. Lee, I.; Kim, M.; Jin, C. Impact of hull flexibility on the global performance of a 15 MW concrete-spar floating offshore wind turbine. *Mar. Struct.* **2025**, *100*, 103724. [CrossRef]
43. Bian, J.; Wan, L.; Yang, Y.; Li, S.; Hao, J.; Xin, J.; Zhang, C. Dynamic response analysis of alternative mooring system designs for a 15 MW floating wind turbine with an emphasize on different limit states. *Ocean Eng.* **2025**, *315*, 119787. [CrossRef]
44. Jeon, T.; Kim, B.-S.; Kim, J.; Paek, I.; Lim, C.-H. Parametric Analysis of Control Techniques for 15 MW Semi-Submersible Floating Wind Turbine. *Appl. Sci.* **2025**, *15*, 519. [CrossRef]
45. Navarro-Martínez, G.; Martínez-Turégano, J.; Blasco-Gimenez, R. Control of a 15MW off-shore wind turbine for black-start operation. *Math. Comput. Simul.* **2025**, *229*, 15–31. [CrossRef]
46. Bozyigit, B.; Bozyigit, I.; Prendergast, L.J. Rapid assessment of seismic performance of large monopile-supported offshore wind turbines under scour. *Eur. J. Mech.-A/Solids* **2025**, *109*, 105451. [CrossRef]
47. He, C.; Sun, T.; Zhang, Z.; Liu, H.; Wang, C.; Wang, J. Numerical investigation on the second-order sum-frequency wave forces induced mooring fatigue of a 15 MW TLP FOWT. *Ocean Eng.* **2025**, *322*, 120463. [CrossRef]
48. Khezri, A.; Park, H.; Lee, D. Numerical Study on the Lateral Load Response of Offshore Monopile Foundations in Clay: Effect of Slenderness Ratio. *Appl. Sci.* **2024**, *14*, 8366. [CrossRef]
49. Gaertner, E.; Rinker, J.; Sethuraman, L.; Zahle, F.; Anderson, B.; Barter, G.; Abbas, N.J.; Meng, F.; Bortolotti, P.; Skrzypinski, W.; et al. *IEA Wind TCP Task 37: Definition of the IEA 15-Megawatt Offshore Reference Wind Turbine*; National Renewable Energy Lab. (NREL): Golden, CO, USA, 2020.

Disclaimer/Publisher's Note: The statements, opinions and data contained in all publications are solely those of the individual author(s) and contributor(s) and not of MDPI and/or the editor(s). MDPI and/or the editor(s) disclaim responsibility for any injury to people or property resulting from any ideas, methods, instructions or products referred to in the content.